

FEASTS: The fate of gas and star formation in interacting galaxies

Shun Wang,¹ Jing Wang,^{1*} Karen Lee-Waddell,^{2,3,4} Dong Yang,¹ Xuchen Lin,¹ and Lister Staveley-Smith^{2,5}

¹Kavli Institute for Astronomy and Astrophysics, Peking University, Beijing 100871, China

²International Centre for Radio Astronomy Research (ICRAR), The University of Western Australia, 35 Stirling Highway, Crawley, WA 6009, Australia

³CSIRO Space & Astronomy, PO Box 1130, Bentley, WA 6102, Australia

⁴International Centre for Radio Astronomy Research (ICRAR), Curtin University, Bentley, WA 6102, Australia

⁵ARC Centre of Excellence for All-Sky Astrophysics in 3 Dimensions (ASTRO 3D), Australia

Accepted XXX. Received YYY; in original form ZZZ

ABSTRACT

We use H_I data from the FAST Extended Atlas of Selected Targets Survey (FEASTS) to study the interplay between gas and star formation of galaxies in interacting systems. We build control and mock H_I disks and parameterize H_I disorder by a series of disorder parameters, describing the piling, clumpiness and expansion of H_I. We find that interacting galaxies have higher H_I disorder described by almost all disorder parameters. Systems with comparable stellar masses and small relative velocities tend to have stronger expansion and clumpiness of H_I. At a given stellar mass, decreased H_I and total neutral gas mass and suppressed star formation rate of secondary galaxies are correlated with most disorder parameters. For primary galaxies, H_I and total neutral gas deficiency correlate with more H_I piling at two ends of the system outside H_I disks but not with the expansion or clumpiness of H_I. We also find that the H_I surface densities of both primary and secondary galaxies are lower within the H_I disks and higher outside compared to the control galaxies. Our results suggest that while all the disorder parameters quantify the interaction strength almost equally well, they have different sensitivities in tracing star formation rate and gas mass enhancements. They also imply that while gas removal likely dominates the tidal effects on secondary galaxies, primary galaxies experience more complex situation that are possibly related to gas depletion and accretion happening at different interaction stages.

Key words: galaxies: interactions – galaxies: ISM – galaxies: intergalactic medium – galaxies: star formation – galaxies: evolution

1 INTRODUCTION

Galaxies in our Universe are not ideally isolated. A large fraction of them reside in groups and clusters with neighbors at low redshift (e.g., Wetzel et al. 2013). In groups and clusters, central galaxies accrete less massive infalling galaxies. And satellites galaxies themselves also interact and even merge with each other. The Λ -Cold Dark Matter (Λ CDM) cosmology predicts that the halo-halo merger is one of the major channel of mass and structure assembly. The continuous merger of massive halos throughout their assembly history further increases the frequency of galaxy-galaxy interaction inside the halos (e.g., Fujita 1998; Gnedin 2003). Tidal interaction between galaxies are thus inevitable and important for understanding the evolution of galaxies in the local Universe.

The effects of tidal interaction have been extensively studied in the literature. Observational studies have focused on: 1) enhanced star formation and its dependence on galaxy separation (e.g., Barton et al. 2000; Ellison et al. 2008), mass ratio (e.g., Woods & Geller 2007; Lambas et al. 2012), primary/secondary identity (e.g., Lambas et al. 2003; Woods & Geller 2007), morphology (e.g., Cao et al. 2016; Zuo et al. 2018), star formation activity (e.g., Woods & Geller 2007; Moon et al. 2019), gas fraction (e.g., Scudder et al. 2015), environment (e.g. Alonso et al. 2004; Ellison et al. 2010), and multiplicity (e.g.,

Bustamante et al. 2020; Garduño et al. 2021), 2) induced gas inflow deduced from metallicity measurements (e.g., Scudder et al. 2012; Ellison et al. 2013), 3) perturbed atomic hydrogen (H_I) (e.g., Pearson et al. 2016; Bok et al. 2019) and whether it is suppressed or enhanced (e.g., Ellison et al. 2015; Zuo et al. 2018; Ellison et al. 2018; Wang et al. 2022), 4) molecular hydrogen (H₂) content (e.g., Pan et al. 2018; Violino et al. 2018) and, 5) the effect of AGN activity (e.g., Ellison et al. 2011) and stellar feedback (e.g., Smith et al. 2019). More recent observations with improved spatial resolution present a more detailed picture (e.g., Thorp et al. 2019). The preference of central star formation enhancement is confirmed, though with a dependence on the stage of interaction (e.g., Pan et al. 2019). The H₂ distribution also tends to be more centrally peaked when the galaxy is experiencing tidal interaction (e.g., Chown et al. 2019).

In particular, there are ongoing debates on how tidal interaction affects the gas content in different populations. In statistical samples of interacting galaxies, e.g., those selected from SDSS, there is no universal agreement regarding the tidal effect on their H_I content. Yu et al. (2022) reported a marginal decrease in H_I gas fraction in major-merger pairs. Ellison et al. (2015) found no evidence of H_I deficiency in post-mergers with ALFALFA (Haynes et al. 2018) data. Ellison et al. (2018) found that the H_I detection rate of post-merger galaxies is significantly higher than that of xGASS (Catinella et al. 2018). And the median H_I gas fraction is ~ 0.5 dex higher than control galaxies with matched stellar masses. Zuo et al. (2018) also found

* E-mail: jwang_astro@pku.edu.cn

that the H I gas fractions of spiral galaxies in close galaxy pairs at $z = 0$ are consistent with the average of spiral galaxies in general. Similar enrichment is also observed for molecular gas as a 0.4 dex enhancement in gas fraction (Violino et al. 2018) and a significant enhancement in gas mass (Pan et al. 2018).

In the specific interacting systems of Hickson compact groups (HCGs, Hickson 1982), on the other hand, H I deficiency was ubiquitously found (e.g., Williams & Rood 1987; Huchtmeier 1997). Such deficiency was confirmed by Martinez-Badenes et al. (2012) with a redshift-limit sample of HCG galaxies. Hess et al. (2017) further found that the H I deficiency of HCG 44 is not accounted for by additional H I gas in the IGM environment revealed by deeper observation, tentatively confirming the speculation of Verdes-Montenegro et al. (2001) that phase transition in the IGM environment following the tidal stripping is responsible for the H I deficiency. On the other hand, Jones et al. (2019) found that HCG 16 as a whole group is not H I deficient after including H I in the IGM environment, suggesting that the evolutionary track of H I in interacting groups may not be unique (Verdes-Montenegro et al. 2001). The molecular gas content in HCG galaxies shows more diversity. It can either be increased (e.g., Martinez-Badenes et al. 2012), decreased (e.g., Verdes-Montenegro et al. 2001) or remain normal (e.g., Verdes-Montenegro et al. 1998).

The diversity of gas deficiency of interacting galaxies may originate from the different strengths or evolutionary stage of the tidal interaction, different initial conditions for the galaxies and pairs/groups, etc. The limitations of different types of observational data may also play a part. Recently, Wang et al. (2023) separate a distinct phase of H I, i.e., diffuse H I, in the interacting NGC4631-NGC4656 system. By comparing FAST data to interferometry data, the authors identified a significant amount of diffuse H I that was previously missed. The flux is missing partly due to the observational sensitivity, but mostly due to the missing zero-spacing in interferometers. Further analysis reveals a close connection between the diffuse H I and IGM. It tends to survive photon ionization and thermal evaporation and induce cooling out of hot IGM. So, the replenishment of ISM by cooling/accretion from IGM via diffuse H I may be directly observed by FAST in such interacting systems. This may be a key to understanding H I enrichment and deficiency in interacting systems.

Thus, we seek to understand the tidal effects on H I content and star formation by studying the interacting galaxy pairs observed in FEASTS (FAST Extended-Atlas-of-Selected-Targets Survey) sample (Wang et al. 2023). These are simpler cases of tidal interaction than those in compact groups. Benefiting from the powerful FAST instrument, we minimize the possible observational effects introduced by limited sensitivity and the problem of missing flux that affects interferometric data. We are also able to well resolve the H I component in these interacting systems so that the spatial distribution of H I can be analyzed.

Our galaxy samples and data are introduced in Section 2. In Section 3 we demonstrate our method of obtaining all the measurements of gas and star formation. The main results of our study are presented in Section 4. We discuss the implications for the fate of gas and star formation in interacting systems in Section 5. Finally, in Section 6 we summarize our main results.

2 SAMPLE AND DATA

2.1 Sample galaxies from FEASTS

FEASTS is a 21-cm emission line survey to map the extended H I in Local Volume galaxies (Wang et al. 2023, 2024). It takes advantage of

the high sensitivity and low sidelobe levels of FAST (Five-hundred-meter Aperture Spherical radio Telescope) in China. It maps the extended and low-surface density H I that is typically missed in interferometric observations, studying the evolution of Local Volume galaxies that have grand H I disks, examining the properties of their ISM, IGM and the related physical connections and processes.

We select eight interacting systems with prominent H I tidal features and ten arbitrary isolated galaxies without optically-confirmed companions within a distance of ~ 100 kpc from the FEASTS sample. They occupy similar parameter space on H I fraction main sequence (HIMS, Janowiecki et al. 2020) and star forming main sequence (SFMS, Saintonge et al. 2016) as most primary galaxies of the interacting sample (Figure 4). There is only one primary galaxy, M77, having significantly higher SFR than the control galaxies for its M_* . We confirm that after removing the M77 associated galaxy pair, the control sample involved results in Section 4.1 and 4.2 remain qualitatively the same. At the least, these isolated galaxies are well representative of normal-star-forming galaxies. These galaxies are listed in Table 1 and 2. We present the moment-0 maps (column density images) and moment-1 maps (velocity fields) of the interacting systems in Figure 1. For NGC3169-NGC3166 and NGC4725-NGC4747 systems, we show the comparison between FEASTS channel maps and moment-0 maps with those from ALFALFA and GMRT observations (Lee-Waddell et al. 2012, 2016) in Appendix A. It is obvious that previous GMRT observation missed a significant amount of large-scale H I fluxes and diffuse H I structures, while ALFALFA observations have higher noise level and worse spatial resolution.

Table 1. Physical properties of galaxies in the interacting systems. Column (1): Identifier of the galaxies. The names of primary galaxies are in bold and the corresponding secondary galaxies are right below them. Column (2)-(3): R.A. and DEC. of the galaxy. Column (4): Heliocentric velocity of the galaxy. Column (5): R_{25} of the galaxy. Column (6): Axis ratio of the galaxy, all from S⁴G. Column (7): Position angle of the galaxy disk, defined as the angle of the semi-major axis in the approaching part of the disk, counting counter-clockwise from north, all from S⁴G. Column (8): Inclination angle of the galaxy derived from axis ratio or cited from the reference noted. Column (9): Distance to the galaxy. Column (10): Log stellar mass of the galaxy. Column (11): Log star formation rate of the galaxy. Column (12): Log H_I mass of the galaxy. Column (13): Log H₂ mass of the galaxy, left blank if not available. Column (14): Log stellar mass ratio between secondary and primary galaxy. Column (15): Absolute relative velocity of the galaxy pair. Column (16): Projected distance between primary and secondary galaxy.

name	R.A. (J2000) (deg)	DEC. (J2000) (deg)	V_{hel} (km s ⁻¹)	R_{25} (arcsec)	b/a	P.A. (deg)	incl. (deg)	Dist. (Mpc)	log M_*/M_{\odot}	log SFR/ M_{\odot} yr ⁻¹	log M_{HI}/M_{\odot}	log M_{H_2}/M_{\odot}	log $M_{*,\text{sec}}/M_{*,\text{prim}}$	$ \Delta V_{\text{los}} $ (km s ⁻¹)	D_{proj} (kpc)
(1)	(2)	(3)	(4)	(5)	(6)	(7)	(8)	(9)	(10)	(11)	(12)	(13)	(14)	(15)	(16)
M77	40.66962	-0.01329	1137	212.40	0.998	-80.0	4	12.30	10.71	1.51	9.10	6.53 ^d	-0.27	141	109.84
NGC1055	40.43847	0.44318	996	227.55	0.571	104.2	86 ^a	12.30	10.44	0.07	9.69	9.53 ^e			
NGC672	26.97699	27.43278	429	217.35	0.455	68.4	65	8.28	9.37	-0.68	9.49	-	-0.57	84	19.49
IC1727	26.87454	27.33335	345	207.55	0.366	151.8	70	8.28	8.80	-0.91	9.28	-			
NGC4631	190.53337	32.54151	610	464.65	0.247	87.1	85 ^b	7.30	10.05	0.30	10.06	9.19 ^f	-1.22	36	68.44
NGC4656	190.99037	32.17037	646	454.05	0.155	214.7	88	7.96	8.83	-0.24	9.80	-			
NGC4725	192.61072	25.50076	1209	321.45	0.705	30.5	48	12.40	10.76	-0.09	9.71	8.74 ^f	-1.34	19	87.97
NGC4747	192.93997	25.77503	1190	104.00	0.374	37.2	70	14.30	9.42	-0.73	9.35	-			
NGC3169	153.56266	3.46609	1232	130.95	0.754	238.4	44	23.70	10.98	0.29	10.26	9.79 ^e	-0.05	49	53.15
NGC3166	153.44053	3.42481	1183	143.60	0.568	81.9	62	23.70	10.93	-0.19	9.72	9.32 ^e			
NGC660	25.75979	13.64568	848	249.55	0.390	183.6	76	9.00	9.79	0.23	9.54	9.31 ^e	-1.62	81	56.80
IC0148	25.61234	13.97703	767	101.65	0.239	227.8	79	9.00	8.17	-1.53	8.70	-			
NGC5775	223.49022	3.54447	1676	125.05	0.511	145.0	86 ^c	19.80	10.47	0.46	9.96	-	-1.06	108	25.41
NGC5774	223.42693	3.58249	1568	90.60	0.842	153.6	33	19.80	9.41	-0.55	9.46	-			
NGC5194	202.46957	47.19526	460	336.60	0.656	175.7	51	8.58	10.73	0.65	9.66	9.46 ^g	-0.37	5	11.02
NGC5195	202.49829	47.26613	455	172.65	0.708	-62.7	49	8.58	10.36	-0.16	8.99	-			

^aSchechtman-Rook & Bershad (2014) ^bHeald et al. (2011) ^cIrwin (1994) ^dHelfer et al. (2003) ^eSorai et al. (2019) ^fSchruba et al. (2012) ^gLeroy et al. (2008)

2.2 FEASTS HI data

The observation setting of FEASTS is described in Wang et al. (2023, 2024), and we briefly summarize it here. The FEASTS HI data is observed using the on-the-fly multi-beam scan mode of FAST. Each target is scanned in both RA and Dec directions for $\sim 1^\circ$ with at least three passes each. The scans were conducted with the L -band 19 beam receiver rotated, so that the effective angular separation between scan lines is $1'.15$. The data is recorded using the *Spec(W+N)* backend with a channel width of 7.63 kHz, or 1.61 km s^{-1} for HI 21-cm observations in the nearby Universe.

Information about new FEASTS observations are shown in Table 3. Observations of NGC628, NGC925, NGC2903, NGC3521, NGC4631, NGC5194 and NGC7331 are presented in Wang et al. (2023, 2024), and those of NGC891, NGC1055, NGC4244, NGC4517 and NGC5775 are presented in Yang et al. (in prep.), which are all part of the FEASTS program.

The data reduction is carried out with a pipeline developed following the standard procedure of reducing radio single-dish data, particularly that from the Arecibo Legacy Fast ALFA Survey (Haynes et al. 2018) and HI Parkes All Sky Survey (Barnes et al. 2001). More detailed description of the data reduction procedure is referred to Wang et al. (2023).

2.3 Archival H2 data

We use the CO observation from HERACLES (Leroy et al. 2009), BIMA (Helfer et al. 2003) and COMING (Sorai et al. 2019) to derive the molecular gas distribution of the galaxies in our interacting systems. Among 16 galaxies in the interacting sample, we have three, one and four CO images of galaxies from HERACLES, BIMA and COMING, respectively (Table 1).

2.4 Ancillary information

The positions of the galaxies ($R.A.$ and $DEC.$) are from the Simbad database and the heliocentric velocities are from the NED database. The optical disk sizes R_{25} are also from the NED database, which are all from the RC3 catalog (de Vaucouleurs et al. 1991). The galaxy T -type¹, axis ratio and position angle of the optical disks are from the S⁴G (Sheth et al. 2010) database when available, and Simbad database otherwise. Inclinations of the galaxies are from various literature (see references in Table 1 and Table 2) when available. Otherwise they are derived from the axis ratio and morphological type following Fouque et al. (1990). We remind the readers to be cautious about the inhomogeneity in these parameters. Distance, stellar mass and star formation rate (SFR) are from the ZOMGS (Leroy et al. 2019) catalog. These physical properties of the interacting and isolated galaxies are shown in Table 1 and Table 2, respectively.

3 ANALYSIS

3.1 Data preparation

3.1.1 Source identification in HI cubes

We use *SoFiA* (Serra et al. 2015) to detect HI emissions from the data cube and generate source masks. The threshold-based

¹ In cases where T -type is from Simbad, we translate ‘SB’, ‘SAB’ and ‘SA’ into T -type = 3, 2, 1, respectively.

smooth+clipping source-finding algorithm is used with the reliability module enabled. More technical details are referred to Wang et al. (2023). The produced source masks are then used to generate moment-0, moment-1 maps and derive the noise level of each data cube. We manually check and confirm there are no floating HI clumps or other tidal features that may originate from interaction outside the selected sources.

Following the procedure of Wang et al. (2023) and Huang et al. (in prep.), we apply the watershed algorithm to the moment-0 maps to separate the HI fluxes of small galaxies from the main galaxies of the interacting pairs (Appendix B). We confirm that including the flux in these pixels does not significantly change the results presented in this work.

3.1.2 Division of HI flux between primary and secondary galaxies

For each interacting system, we denote the galaxy that has larger stellar mass as primary galaxy and the other as secondary galaxy. We divide the HI fluxes of the two galaxies by deciding a 2D boundary upon which a test mass experiences equal strength of tidal torque influence (Elmegreen et al. 1991) from them. The boundary is a circle of Apollonius on the sky plane defined by center C (Equation 1) and radius R (Equation 2). The HI flux inside the circular boundary is assigned to the secondary galaxy and the flux outside is assigned to the primary.

$$C = \left(\frac{X_{\text{prim}} - k^2 X_{\text{sec}}}{1 - k^2}, \frac{Y_{\text{prim}} - k^2 Y_{\text{sec}}}{1 - k^2} \right) \quad (1)$$

$$R = \frac{k}{1 - k^2} d_{\text{prim2sec}} \quad (2)$$

$$k \equiv \frac{d_{\text{prim}}}{d_{\text{sec}}} = \left(\frac{M_{\text{prim}}}{M_{\text{sec}}} \right)^{\frac{1}{3}} \quad (3)$$

$(X_{\text{prim}}, Y_{\text{prim}})$ and $(X_{\text{sec}}, Y_{\text{sec}})$ are the coordinates of the two galaxies on the sky, k is the ratio of the distances from any point on the circle to the two galaxies, and d_{prim2sec} is the distance between the two galaxies.

Note that there are multiple factors resulting in uncertainty in flux division, including projection effects and neglected orbital history of the system. And such division does not reflect the origin of gas, for HI flux assigned to a galaxy can be either from its own HI disk, the companion or even cooling induced in CGM. These uncertainties propagate to following analysis that is based on the HI mass measurements performed here.

3.2 Constructing comparison images

3.2.1 Construction of control HI disks

We use the HI disks of isolated FEASTS galaxies (Section 2.1) to construct control HI disks as follows:

(i) For each interacting galaxy, isolated galaxies with matched inclinations (either $incl. < 50^\circ$, $50^\circ < incl. < 80^\circ$ or $incl. > 80^\circ$) are selected.

(ii) The HI disks of the selected isolated galaxies are enlarged, so that the enlarged HI disks have the same apparent size as that of the interacting galaxy.

Table 2. Physical properties of the isolated galaxies. Column (1): Identifier of the galaxies. Column (2)-(3): R.A. and DEC. of the galaxy. Column (4): Axis ratio of the galaxy from S⁴G, or Simbad where noted. Column (5): Position angle of the galaxy disk, defined as the angle of the semi-major axis of the approaching part of the disk, counting counter-clockwise from north. From S⁴G, or Simbad where noted. Column (6): Inclination angle of the galaxy derived from axis ratio, or cited from the reference noted. Column (7): Distance to the galaxy. Column (8): Log stellar mass of the galaxy. Column (9): Log H I mass of the galaxy. Column (10): Log star formation rate of the galaxy.

name	R.A. (J2000)	DEC. (J2000)	b/a	P.A.	incl.	Dist.	log M_*/M_\odot	log M_{HI}/M_\odot	log SFR/ $M_\odot \text{ yr}^{-1}$
(1)	(2)	(3)	(4)	(5)	(6)	(7)	(8)	(9)	(10)
NGC891	35.63711	42.34832	0.199 ^c	202.0 ^c	84 ^a	9.91	10.72	9.72	0.32
NGC4517	188.18994	0.11504	0.178	261.6	84	11.10	10.22	9.66	-0.15
NGC3344	160.87979	24.92222	0.900	-58.6	27	10.00	10.29	9.75	-0.08
NGC4559	188.99017	27.95996	0.421	-37.0	67	8.91	9.81	9.83	-0.18
NGC7331	339.26688	34.41578	0.398 ^c	171.0 ^c	76	14.70	11.00	10.13	0.53
NGC2903	143.04213	21.50083	0.492	199.4	63	8.47	10.42	9.66	0.32
NGC628	24.17394	15.78364	0.840	118.0	34	9.77	10.24	10.11	0.23
NGC925	36.82047	33.57888	0.549 ^c	282.0 ^c	61	9.16	9.75	9.82	-0.17
NGC3521	166.45237	-0.03590	0.566	-18.5	73 ^b	11.20	10.83	10.03	0.42
NGC4244	184.37358	37.80711	0.188	225.1	90 ^a	4.29	9.20	9.32	-0.95

^aHeald et al. (2011) ^bWalter et al. (2008) ^cfrom Simbad

Table 3. Basic information about new FEASTS observations of the sample systems and galaxies. Column (1): Identifier of the systems or galaxies. Column (2)-(3): R.A. and DEC. of the field center. Column (4): Size of the Field-of-View. Column (5): The date of observation. Column (6): The effective integration time per l-o-s. Column (7): The noise level of the data cube. Column (8): The corresponding detection limit assuming 20 km s⁻¹ line widths and 3 – σ signal.

name	R.A. (J2000)	DEC. (J2000)	FoV	obs. date	int. time per beam	noise	depth
(1)	(2)	(3)	(deg × deg)	(YYYYMMDD)	(s)	(mJy beam ⁻¹)	(10 ⁻¹⁷ cm ⁻²)
NGC672-IC1727	26.9211	27.3887	1.2° × 1.2°	20221115	221.6	0.95	4.74
NGC4725-NGC4747	192.7470	25.6636	1.5° × 1.5°	20220329	229.0	0.89	4.50
NGC3169-NGC3166	153.6215	3.4505	1.5° × 1.5°	20220306	207.1	1.12	5.62
NGC660-IC0148	25.7590	13.6420	1.0° × 1.0°	20211115	214.4	0.95	4.77
NGC3344	160.8796	24.9237	1.2° × 1.2°	20220327	229.8	1.01	5.07
NGC4559	188.9893	27.9614	1.2° × 1.2°	20220425	235.9	1.01	5.07

(iii) The enlarged H I disks are further rotated to match the position angles of the interacting galaxy. Two rotated disks can be produced based on one enlarged H I disk (rotated by 180°).

(iv) Finally, moment-0 maps of all possible combinations of the rotated H I disks for interacting galaxies are produced.

A number of $N_{\text{control}} = 4 \times N_{\text{prim}} \times N_{\text{sec}}$ control moment-0 maps are produced for each system, where N_{id} ($\text{id} = \text{prim}, \text{sec}$) is the number of isolated galaxies in the corresponding inclination bin for the primary and secondary galaxy, respectively. N_{control} ranges from 24 to 100 for all the interacting systems in our sample. We do not use H I disks observed with interferometry in the literature, so that the possible effects of the missing flux problem are avoided.

3.2.2 Construction of mock HI disks

We use the *GALMOD* module of ^{3D}BAROLO (Di Teodoro & Fraternali 2015) to construct mock H I disks to see how an ‘average’ H I disk would look like if observed under the same conditions. They will serve as reference or baseline images to be subtracted for highlighting and characterization of abnormal H I morphology in the interacting system images and in the control images (Section 3.3.1). We note that, these averaged disks are based on previous characterization with the interferometry data, and thus do not necessarily represent the average of H I disks detected in FEASTS, which will be studied with larger samples in the future (Wang et al. in prep).

The size of the H I disk (R_{HI}) is derived based on the H I size-mass relation (Wang et al. 2016). We linearly extrapolate the universal H I radial profile out to $2R_{\text{HI}}$ following the extrapolation performed in Wang et al. (2020), and use it as the radial distribution of the mock H I disks (with a small adjustment, Appendix C). The scale height of the mock H I disks is set as a function of distance to the disk center, going up linearly from 0.1 kpc at the center to 0.6 kpc at a radius of 20 kpc and flattens at larger radii. Such functional form is determined as a simplified average of those derived in Bacchini et al. (2019a,b, 2020).

The rotation curves of the mock H I disks are assigned according to their baryonic masses. We divide SPARC galaxies (Lelli et al. 2016) into five different baryonic mass bins and derive a median rotation curve out to the radius at which we still have measurements of the rotational velocities for more than half galaxies in each bin. The rotation curves are assumed to be flat beyond this range. The median rotation curves are smoothed before assigned to the mock H I disks in the corresponding baryonic mass bin. We additionally scale the rotation curve in some cases so that the H I flux distribution of mock in PSD (Figure 2) matches the sample galaxies reasonably well.

^{3D}BAROLO then produces data cubes based on these input. After convolving the channel maps with the average FAST beam (Wang et al. 2023), we obtain the moment images and fluxes via the same procedure as the reduction of FEASTS data. Mock moment-0 maps are obtained for each interacting system by putting the two corresponding mock H I disks on the same image. Similar mock maps

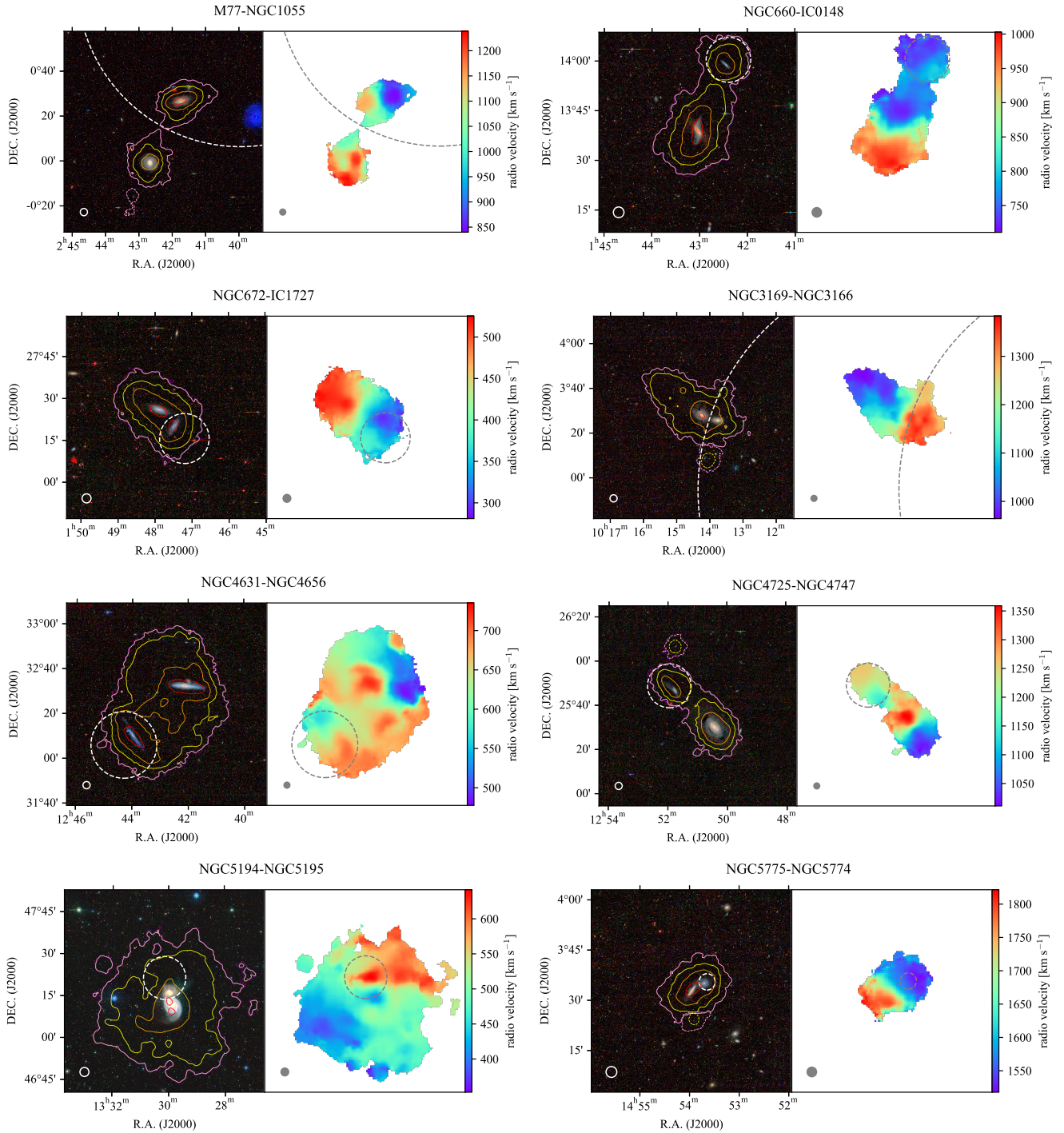


Figure 1. Optical images with H I column density contours overlaid and H I moment-1 maps of the eight interacting systems. The optical images are from DESI Legacy Survey. The contour levels are $5 - \sigma$ detection limit (purple, assuming 20 km s^{-1} line widths), 10^{18} (pink), 10^{19} (yellow), 10^{20} (orange) and 10^{21} (red) cm^{-2} . The solid contours enclose fluxes of the main H I component of the systems. The dashed contours enclose H I fluxes of small galaxies separated from the main H I component of the systems (Section 3.1.1). The white (in optical images) and gray (in moment-1 maps) dashed circles are the boundaries determined for H I flux division between the primary and secondary galaxies (Section 3.1.2).

are produced for the images of control galaxies. The mock H I disks of control galaxies are enlarged and rotated in the same way as we treat the controls (Section 3.2.1). We note that mocks only represent the average, i.e., no scatter around this average is simulated (radial profile, scale height and rotation curve), which may give rise to systematic uncertainties in our sample. And the assumed H I radial

profile is derived from interferometry data, which may suffer from the missing flux problem (Wang et al. 2023).

We present H I PSDs of the interacting galaxies in Figure 2 with contours of the real and mock PSD overlaid. In all eight interacting systems, the H I distribution show different level of deviation from

that of the mock. In Appendix D we present a detailed description of these HI PSDs.

3.3 Parametrization and measurements

3.3.1 Disorder parameters

We characterize disorder in the HI morphologies using the moment-0 and the residual maps. The residual maps are constructed by subtracting mock moment-0 maps from the FEASTS and the control moment-0 maps. An illustration of the regions in the residual maps is shown in Figure 3, which is produced as follows:

We firstly rotate the residual maps so that the primary galaxy is on the left of the secondary galaxy. Next, we plot two 45° lines extending from the center of the primary galaxy to the left, and two from the center of the secondary galaxy to the right. Finally, we plot the contour of detected HI fluxes at a column density of 10^{18} cm^{-2} . We also plot the HI disk regions with semi-major axis set to R_{HI} , and position angles and axis ratios determined by the optical photometry (Section 2.4).

The rotated residual maps of the interacting systems are presented in Section 4.1 and Figure 5 therein. To quantify disorder in the HI morphologies and enable further analysis of their dependence and impact on galactic properties, we measure the HI flux F in the moment-0 maps, the residual HI flux R and the fraction of positive pixels f^+ in the residual maps in the following regions:

- The entire region labeled as detected sources in *SoFiA* source mask (region enclosed by thin solid gray contour in Figure 3). Quantities derived in this region are denoted by subscript tot .
- The region labeled as detected sources in *SoFiA* source mask, with two HI disks excluded ($A_1 \cup A_2 \cup A_3$ in Figure 3). Quantities derived in this region are denoted by subscript $_{123}$.
- The region labeled as detected sources in *SoFiA* source mask at two ends of the system, with two HI disks excluded ($A_1 \cup A_2$ in Figure 3). Quantities derived in this region are denoted by subscript $_{12}$.

Finally the following parameters are calculated, among which $\frac{R_{123}}{F_{123}}$, $\frac{F_{123}}{F_{\text{tot}}}$ and f_{123}^+ quantify the level of HI piling outside HI disks, and $\frac{R_{12}}{F_{12}}$, $\frac{F_{12}}{F_{\text{tot}}}$, $\frac{F_{12}}{F_{123}}$, $\frac{R_{12}}{F_{123}}$ and f_{12}^+ quantify the level of HI piling at two ends of the system outside HI disks:

- $\frac{R_{123}}{F_{123}}$, the fraction of residual flux outside HI disks.
- $\frac{R_{12}}{F_{12}}$, the fraction of residual flux at two ends of the systems.
- $\frac{F_{123}}{F_{\text{tot}}}$, the fraction of fluxes outside the HI disks.
- $\frac{F_{12}}{F_{\text{tot}}}$, the fraction of fluxes at two ends of the systems.
- $\frac{F_{12}}{F_{123}}$, the ratio between fluxes at two ends of the systems to fluxes outside the HI disks.
- $\frac{R_{12}}{F_{123}}$, the ratio between residual flux at two ends of the systems to fluxes outside the HI disks.
- f_{123}^+ , the fraction of positive pixels outside HI disks.
- f_{12}^+ , the fraction of positive pixels at two ends of the systems.

In addition, we derive a disorder parameter L describing the physical extent of HI. It is calculated as:

$$L \equiv \sqrt{L_{\text{R.A.}} \times L_{\text{DEC.}}} / (R_{\text{HI,prim}} + R_{\text{HI,sec}}) \quad (4)$$

where $L_{\text{R.A.}}$ and $L_{\text{DEC.}}$ are the numbers of pixels with HI column densities higher than a uniform detection limit of 10^{18} cm^{-2} in *R.A.* and *DEC.* directions, respectively. And $R_{\text{HI,prim}}$ and $R_{\text{HI,sec}}$ are the HI disk sizes of the primary and secondary galaxies, respectively.

We also derive a disorder parameter S which measures the clumpiness of HI beyond the HI disk. It is defined as the ratio of the sum of the absolute pixel values in the residual map and the sum of the pixel values in moment-0 map, with the pixels inside the two HI disks excluded (Equation 5).

$$S \equiv \frac{\sum_{\text{pix}} |\text{residual map}|}{\sum_{\text{pix}} \text{moment} - 0 \text{ map}} \quad (5)$$

All these parameters are viewed as measurements of disorder of the HI morphologies and referred to as disorder parameters. And they are also measured from the controls. We further derive the difference between those of the interacting system and the median value of the controls. The difference is denoted as $\Delta(X)$, where X is any disorder parameter described above. In particular, we refer to $\Delta(L)$ as the expansion of HI and $\Delta(S)$ as the clumpiness of HI.

3.3.2 Gas surface density profile

We derive the gas surface density profiles of the interacting galaxies. Both HI and H₂ profiles are measured from the corresponding moment-0 maps following a standard procedure of aperture photometry using annulus with increasing radius and fixed ellipticity and position angle determined in the optical. The same procedure is applied to the mocks and controls as well. We further derive the median profiles of controls for each interacting galaxy.

For HI profiles we confirm that excluding pixels belonging to the other galaxy (Section 3.1.2) does not significantly change the results. And we note the systematic uncertainty introduced by inclination and spatial resolution which influence HI observations more severely than those of H₂.

3.3.3 Evaluation of SFR enhancement and HI excess

We define the HI excess ($\Delta \log M_{\text{HI}}$) as follows:

$$\Delta \log M_{\text{HI}} \equiv \log M_{\text{HI}} - \log M_{\text{HI,MS}}(M_*) \quad (6)$$

where $M_{\text{HI,MS}}(M_*)$ is the HI mass predicted by HIMS.

The enhancement of SFR ($\Delta \log SFR$) is derived as Equation 7.

$$\Delta \log SFR \equiv \log SFR - \log SFR_{\text{MS}}(M_*) \quad (7)$$

where $SFR_{\text{MS}}(M_*)$ is the SFR predicted by SFMS. We then refer to interacting galaxies with $\Delta \log SFR > 0$ as star formation enhanced galaxies. Interacting galaxies with $\Delta \log SFR < 0$ are referred to as star formation suppressed galaxies. We have six galaxies that are star formation enhanced and ten that are star formation suppressed. More than half of the primary galaxies are star formation enhanced and most of the secondary galaxies are star formation suppressed. The locus of the interacting and isolated galaxies on SFMS and HIMS are shown in Figure 4.

In order to evaluate the change of gas reservoir caused by tidal interaction and take into account the effect of HI-to-H₂ phase transition, we parameterize the excess of total neutral gas as the corrected HI excess ($\Delta \log M_{\text{HI,cor}}$, Equation 8 and 9).

$$\Delta M_{\text{HI,cor}} = \Delta M_{\text{HI}} + \Delta M_{\text{H}_2} \quad (8)$$

$$\Delta \log M_{\text{HI,cor}} = \log \left[\frac{\Delta M_{\text{HI,cor}}}{M_{\text{HI,MS}}(M_*)} + 1 \right] \quad (9)$$

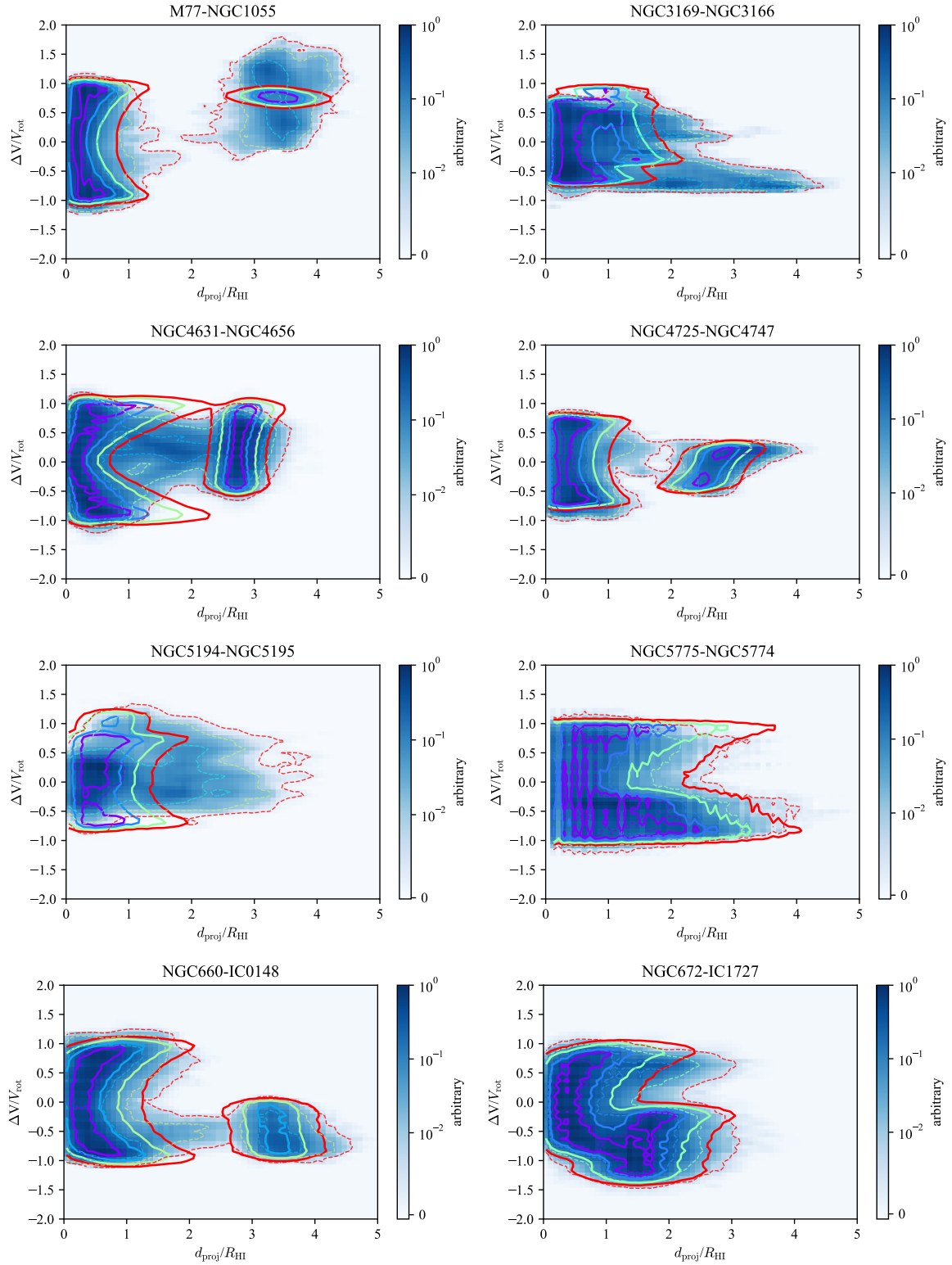


Figure 2. H I PSD of the interacting systems with contour of mock and real PSD overlaid. The projected distance d_{proj} is normalized by R_{HI} and the relative velocity ΔV is normalized by V_{rot} of the reference galaxy. The reference galaxy is the primary galaxy except for the NGC1055-M77 system where it is the secondary galaxy. The pixel sizes are determined individually for each system. The pixel values are all normalized so they peak at unity in each PSD. The solid and dashed contours enclose 99.7% (red), 97.5% (green), 84.1% (blue) and 50% (purple) fluxes of the mock and real PSD, respectively.

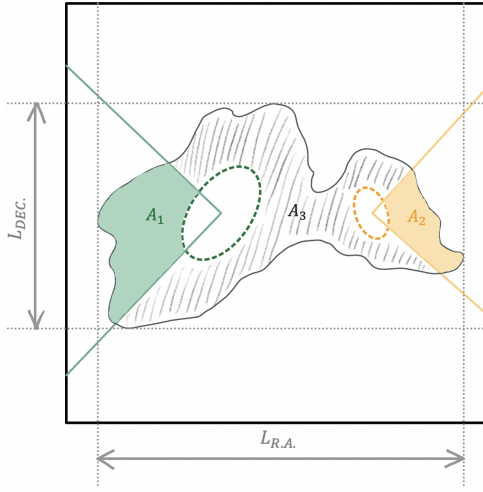


Figure 3. A cartoon illustrating the definition of different regions. Symbols in green and orange are related to primary and secondary galaxy, respectively. HI disks are shown as dashed ellipses. The solid lines enclose the regions at two ends of the system. Regions denoted as A_1 and A_2 are highlighted in green and orange, respectively. Region denoted as A_3 is hatched. The thin solid gray curve outlines the source mask produced by *SoFia*.

where $\Delta M_{\text{HI}} = M_{\text{HI}} - M_{\text{HI,MS}}(M_*)$ and $\Delta M_{\text{H}_2} = M_{\text{H}_2} - M_{\text{H}_2,\text{MS}}(M_*)$. $M_{\text{H}_2,\text{MS}}(M_*)$ is the expected average H_2 mass at a given stellar mass (Saintonge et al. 2017). The excess of H_2 (ΔM_{H_2}) is estimated with ΔSFR based on the best-fit scaling relation between $\Delta \log M_{\text{H}_2}$ and $\Delta \log \text{SFR}$ (Equation 10), with data taken from the xCOLD GASS project (Saintonge et al. 2017).

$$\Delta \log M_{\text{H}_2} = 0.515 \times \Delta \log \text{SFR} + 0.078 \quad (10)$$

A positive/negative gas mass excess is interpreted as the gas being over-abundant/deficient, thus being accreted/depleted. We note that estimating the H_2 excess and corrected HI excess based on scaling relations basically assumes quasi-equilibrium systems, which is unlikely true for interacting and possibly starbursting galaxies. The estimation should thus only be taken as a first-order approximated, statistical view of the connection between HI, H_2 and SFR.

4 RESULTS

4.1 HI disorder caused by tidal interaction

In Figure 5 we present the rotated residual maps. We see obvious negative regions (pixels in red) around the center of the galaxies in almost all interacting systems. And the pixels tend to be blue rather than red outside the HI disks, especially at two ends of the system. While for the residual maps of the controls (Appendix E), the central regions are positive (pixels in blue) in most cases. The outskirts of the HI disks are generally red, occasionally with blue pixels outside the hashed regions. Such differences beyond HI disks are captured by the disorder parameters that we defined in Section 3.3.1.

We find significant difference in disorder parameters (Section 3.3.1) between the interacting systems and the controls. We use the K-S test to evaluate the significance of the difference in disorder parameter between interacting systems and controls. The uncertainty of the significance is estimated via bootstrap. In each bootstrap, we randomly extract one control for each interacting system and obtain an equal-size sample of disorder parameter for the controls. We then

record the p-value of the K-S test between this extracted control sample and the interacting system sample. We repeat this procedure for 10,000 times and obtain a distribution of p-value. We take the median and the standard deviation of this distribution as the significance of the difference and the corresponding uncertainty. As shown in Figure 6, f_{12}^+ , f_{123}^+ , $\frac{F_{12}}{F_{\text{tot}}}$, $\frac{F_{123}}{F_{\text{tot}}}$, $\frac{R_{12}}{F_{12}}$, $\frac{R_{123}}{F_{123}}$, $\frac{R_{12}}{F_{123}}$ and $\Delta(L)$ are higher in interacting systems. Thus the disorder parameters successfully characterize disorder in HI morphologies. The HI in interacting systems preferentially piles outside the HI disks, especially at two ends of the systems. And they tend to be more extended compared to those of the controls. On the other hand, the differences in $\frac{F_{12}}{F_{123}}$ and $\Delta(S)$ are not significant (significance > 0.1).

We further study the dependence of HI morphological disorder on the configuration of tidal interaction by searching for correlations between disorder parameters and physical parameters directly related to tidal interaction. The tidal interaction parameters include stellar mass ratios, projected distances and relative line-of-sight (l-o-s) velocities between the secondary and primary galaxies. We measure the significance of the correlations between disorder parameters and galactic properties using the Pearson R coefficient and the corresponding p-value. The uncertainties are also obtained via bootstrap. A summary of these statistics can be found in Table 4. In Figure 7 we present the most significant correlations, which are for the clumpiness and the expansion of HI:

- (i) $\Delta(S)$ (Equation 5) anti-correlates with the relative l-o-s velocity ΔV_{los} . It is also significant if we normalize ΔV_{los} by the maximum rotational velocity (V_{rot}) of either primary or secondary galaxy.
- (ii) $\Delta(L)$ (Equation 4) correlates with the stellar mass ratio between secondary and primary galaxies ($\log M_{*,\text{sec}}/M_{*,\text{prim}}$).

These correlations show that both the relative velocities and the mass ratios between galaxies in the interacting systems strongly influence the HI disorder. The first correlation shows that the clumpiness of HI increases when the two galaxies are closer in the velocity domain. This correlation is also significant (p-value < 0.05) if Spearman or Kendall test is used. And the second correlation shows that the expansion of HI increases when the two galaxies have more similar stellar masses. This correlation is not significant if Spearman or Kendall test is used. Interestingly, we do not observe any significant correlations between HI piling parameters ($\Delta(\frac{F_{12}}{F_{123}})$, $\Delta(\frac{R_{12}}{F_{123}})$, $\Delta(\frac{F_{123}}{F_{\text{tot}}})$, $\Delta(\frac{F_{12}}{F_{\text{tot}}})$, $\Delta(\frac{R_{12}}{F_{12}})$, $\Delta(\frac{R_{123}}{F_{123}})$, $\Delta(f_{12}^+)$ and $\Delta(f_{123}^+)$) and tidal interaction parameters. It implies that the piling of HI outside HI disks may depend more on other tidal interaction properties not quantified here, like the stage of interactions.

4.2 Effects of tidal interaction on gas content and star formation rate

We explore the effects of tidal interaction on the gas content and star formation rate of the galaxies by examining correlations between gas excess, SFR excess and the disorder parameters. In Table 5 we present the Pearson R coefficients and p-value for all the combinations of correlations, for primary galaxies and secondary galaxies, respectively. For primary galaxies, there are significant (p-value < 0.05) anti-correlations for the HI excess ($\Delta \log M_{\text{HI}}$) with $\Delta(\frac{R_{12}}{F_{12}})$. The corrected HI excess ($\Delta \log M_{\text{HI,cor}}$) anti-correlates with $\Delta(\frac{R_{12}}{F_{123}})$ and $\Delta(f_{12}^+)$. These significant correlations are shown in Figure 8, highlighting the connection between HI dragged outside HI disks onto the two ends of the system and the deficiency in HI and total neutral gas for primary galaxies. However, the p-value of the correlations have large uncertainties, reflecting the trends to be primarily driven by a

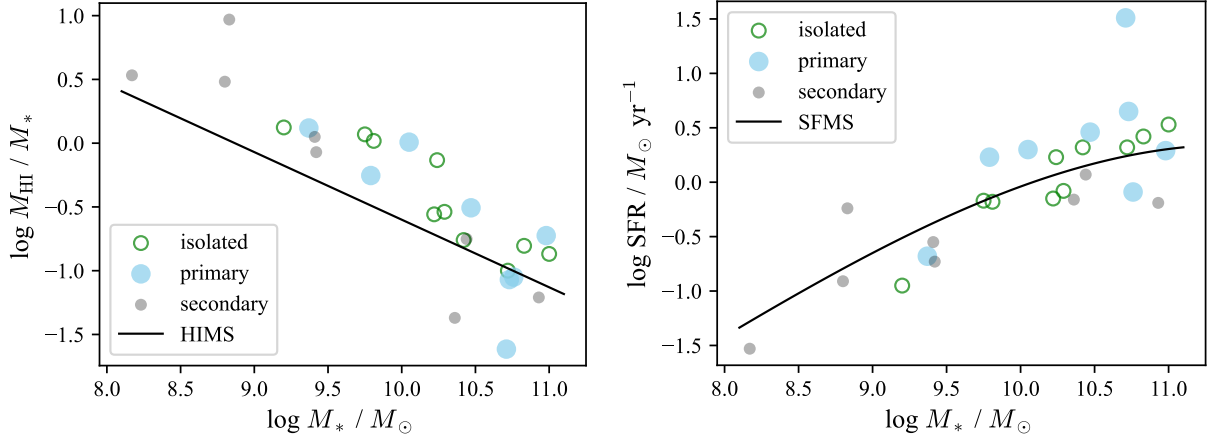


Figure 4. FEASTS interacting and isolated galaxies on H I fraction main sequence (HIMS, left panel) and star forming main sequence (SFMS, right panel). The primary galaxies are shown as large blue circles while the secondary galaxies are shown as small gray circles. The isolated galaxies are represented by open green circles. The corresponding main sequence are plotted as black curves.

Table 4. Significance of the correlations between H I disorder and tidal interaction parameters. The Pearson R coefficient is shown for each correlation, with the corresponding p-value in the following parenthesis. The values for correlations with p-value < 0.10 are highlighted in bold.

	$\log M_{*,\text{sec}}/M_{*,\text{prim}}$	ΔV_{los}	D_{proj}
$\Delta(\frac{F_{12}}{F_{123}})$	0.00(1.00)	0.08(0.85)	0.46(0.26)
$\Delta(\frac{R_{12}}{F_{123}})$	0.47(0.24)	-0.14(0.75)	-0.21(0.62)
$\Delta(\frac{F_{123}}{F_{\text{tot}}})$	0.39(0.34)	-0.48(0.22)	-0.21(0.62)
$\Delta(\frac{F_{12}}{F_{\text{tot}}})$	0.32(0.44)	-0.37(0.36)	0.01(0.99)
$\Delta(\frac{R_{12}}{F_{12}})$	0.57(0.14)	0.17(0.69)	0.16(0.71)
$\Delta(\frac{R_{123}}{F_{123}})$	0.38(0.35)	-0.13(0.76)	-0.39(0.35)
$\Delta(f_{12}^+)$	0.48(0.23)	0.11(0.79)	-0.01(0.98)
$\Delta(f_{123}^+)$	0.53(0.18)	0.14(0.75)	-0.18(0.66)
$\Delta(S)$	0.25(0.55)	-0.82(0.01)	-0.21(0.62)
$\Delta(L)$	0.69(0.06)	-0.23(0.58)	-0.13(0.75)

few galaxies and caution on the significance of the correlations. We also note that these correlations for primary galaxies are not significant based on Spearman or Kendall tests (Appendix F). And we see significant anti-correlation between star formation rate enhancement and $\Delta(\frac{F_{12}}{F_{123}})$ if Spearman test is used.

For secondary galaxies, both H I excess and corrected H I excess significantly anti-correlate with $\Delta(\frac{R_{12}}{F_{123}})$, $\Delta(\frac{F_{123}}{F_{\text{tot}}})$, $\Delta(\frac{R_{12}}{F_{12}})$, $\Delta(\frac{R_{123}}{F_{123}})$, $\Delta(f_{12}^+)$, $\Delta(f_{123}^+)$ and $\Delta(L)$. They are strongly related to the piling of H I outside disks and H I expansion, but not with the H I clumpiness. The star formation rate enhancement also show significant anti-correlation with $\Delta(\frac{R_{12}}{F_{123}})$, $\Delta(\frac{F_{123}}{F_{\text{tot}}})$, $\Delta(\frac{F_{12}}{F_{\text{tot}}})$, $\Delta(\frac{R_{12}}{F_{12}})$, $\Delta(f_{12}^+)$ and $\Delta(f_{123}^+)$. They are mostly linked with the piling of H I outside disks. The H I piling outside H I disks is a sensitive probe for change in H I abundance and star formation levels for secondary galaxies. Using Spearman or Kendall tests generally only produces slightly different p-values for H I excess and corrected H I excess correlations (Appendix F). Except for that $\Delta(\frac{R_{12}}{F_{123}})$ is not significantly correlated with either H I excess or corrected H I excess. Nearly half of the disorder parameters that originally show significant Pearson correlations become insignificantly correlated with SFR enhancements when using Spearman or Kendall tests. The different levels of robustness suggest that H I abundances respond more closely to H I disorder levels than the star formation rates.

4.3 Gas distribution in interacting systems

In Figure 9 we present the median H I surface density profile of the interacting galaxies and the controls. The median H I profiles of primary and secondary galaxies are separately shown. The y-axis represents the surface density ratio between the interacting galaxies and the mock ($\log \Sigma_{\text{HI}}/\Sigma_{\text{HI, mock}}$), so that the difference between a real interacting galaxy and an idealized mock is also highlighted.

We find that firstly, between 0.75 and 1.25 R_{HI} , both interacting galaxies and control galaxies show negative offsets of ~ 0.1 dex from the mock galaxies, reflecting possible systematic bias when constructing the mock galaxies based on previous interferometric measurements, or the relatively small control sample size. But at smaller and larger radius, the interacting and control galaxies show contrary offsets with respect to the mock galaxies, reflecting real differences between these two types of galaxies. While the controls of both primary and secondary galaxies have significantly higher H I surface density than the mocks at $R/R_{\text{HI}} \lesssim 0.75$, interacting galaxies show significant suppression of H I surface density. And the H I surface density of both primary and secondary galaxy are significantly higher than those of the controls at $R/R_{\text{HI}} \gtrsim 1.25 - 1.5$. This suggests that interacting galaxies have less H I inside and more outside their H I disks.

These trends of gas surface density are further studied in Figure 10

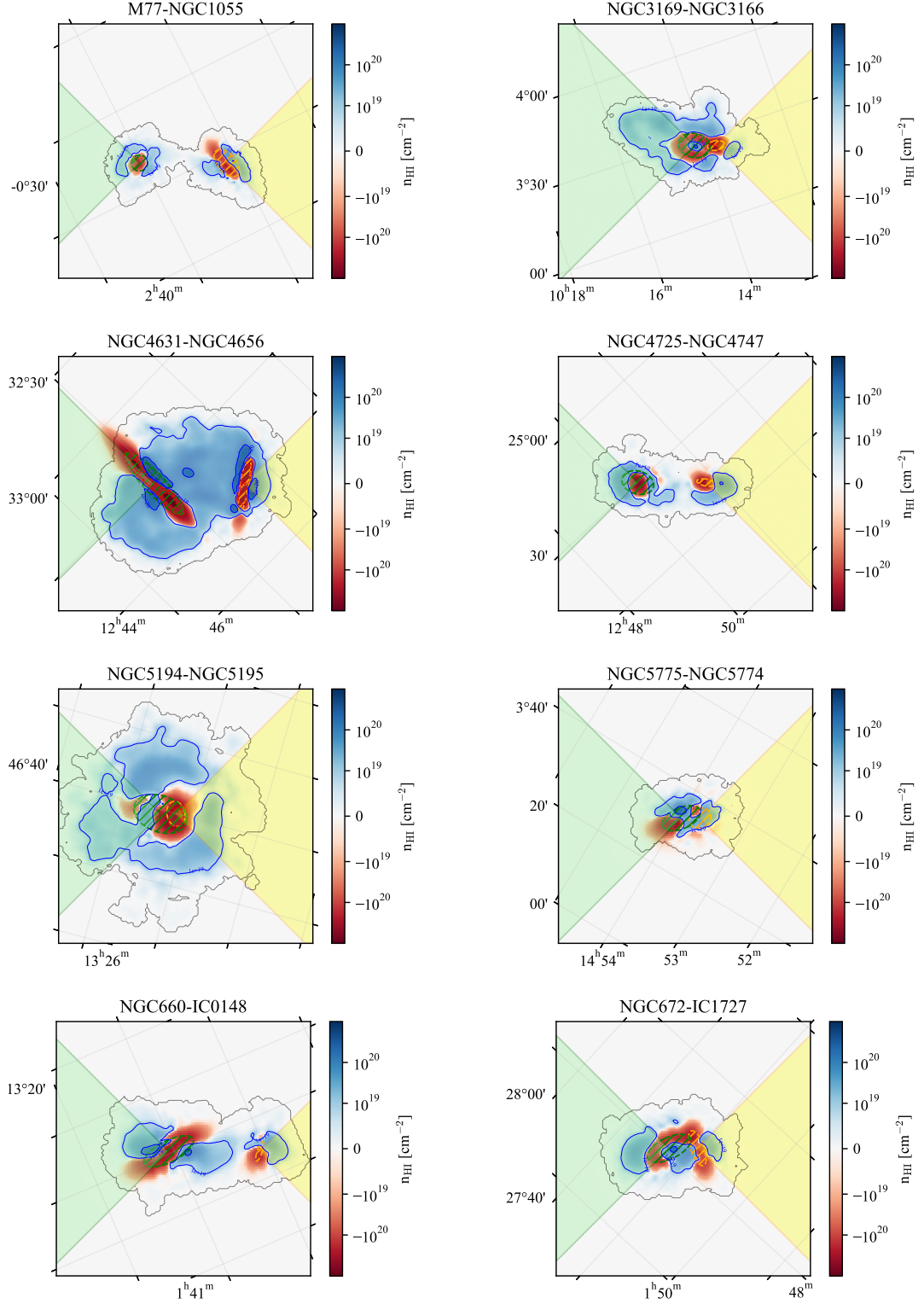


Figure 5. The rotated residual maps of the interacting systems. The gray contour encloses pixels with column densities above 10^{18} cm^{-2} . Blue pixels indicate positive residuals, while red ones indicate negative residuals. The blue and red contours show the values of positive and negative residuals with labels, respectively. The green and orange hatched regions are HI disks of primary and secondary galaxies. The regions at two ends of the system are shaded in green (connected to the primary galaxy) and yellow (connected to the secondary galaxy).

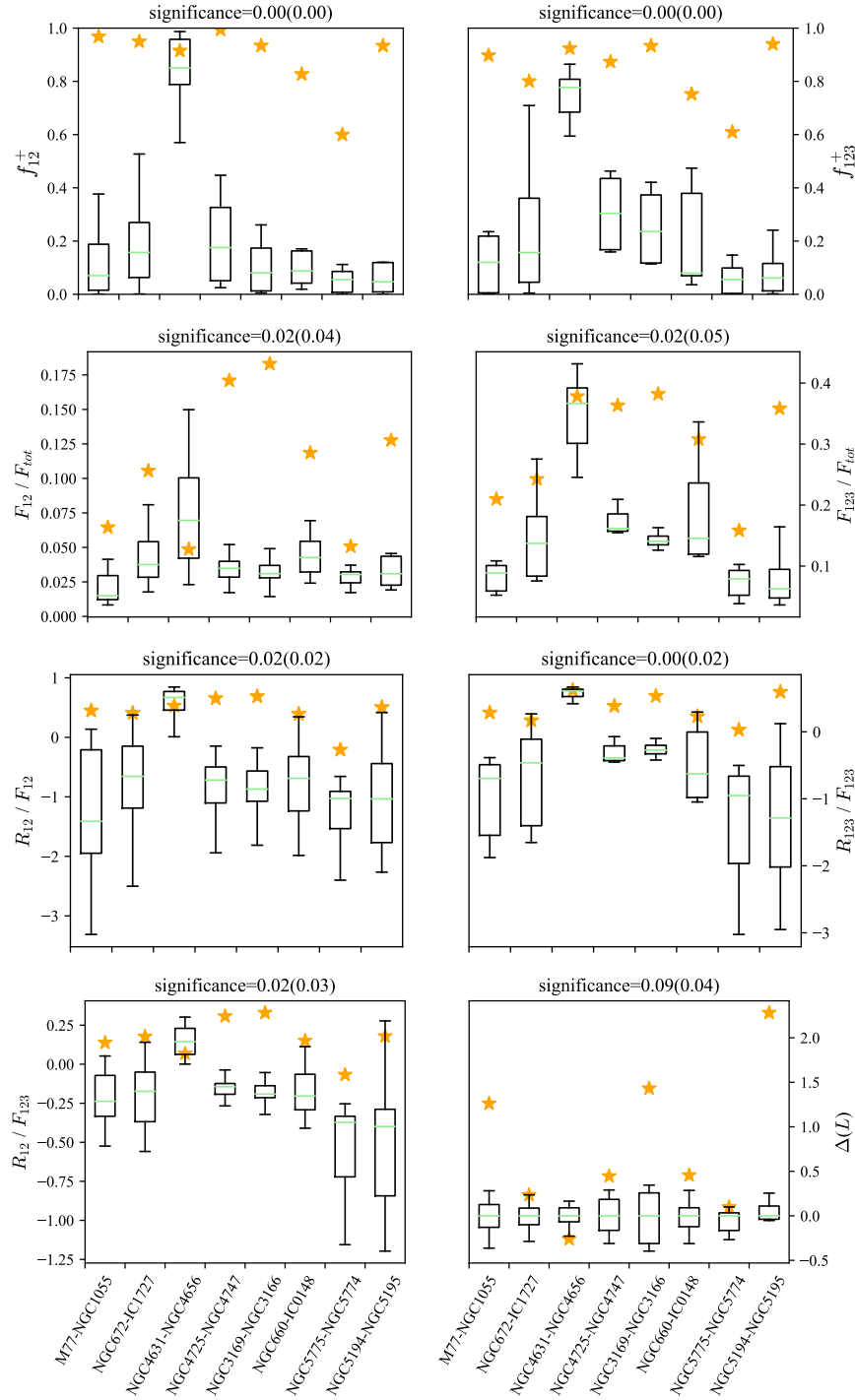


Figure 6. The comparison between disorder parameters of the interacting systems and those of the controls. **Top row:** The fraction of positive pixels at two ends of the system (f_{12}^+) and outside the HI disks (f_{123}^+). **Second row:** The fraction of fluxes at two ends of the system (F_{12}/F_{tot}) and outside the HI disks (F_{123}/F_{tot}). **Third row:** The fraction of residual flux at two ends of the system (R_{12}/F_{12}) and outside the HI disks (R_{123}/F_{123}). **Bottom row:** The ratio between residual flux at two ends of the systems to fluxes outside the HI disks (R_{12}/F_{123}) and the expansion of HI ($\Delta(L)$). On the top of each figure, the significance of the difference is shown with the uncertainty in the following parenthesis. The orange stars represent the parameter values of the interacting systems. The error bars of disorder parameters are all well smaller than the symbols. The black boxes indicate the distribution of the disorder parameter derived from the controls. The box extends from 25- to 75-percentile of the distribution with a green line at the median. The whiskers extend from the box by 1.5 times the difference between 25- and 75-percentile.

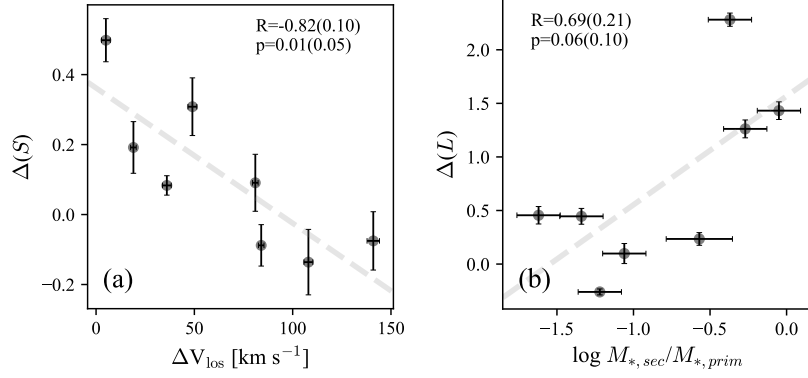


Figure 7. Correlations between disorder parameters and properties of interaction. **Panel (a):** The anti-correlation between $\Delta(S)$ and ΔV_{los} . **Panel (b):** The correlation between $\Delta(L)$ and $\log M_{*,\text{sec}}/M_{*,\text{prim}}$. The Pearson R coefficients and p-values are shown in the upper corners with the bootstrap uncertainties in the following parenthesis. The gray dashed lines are linear fit of the data points, for guiding the eye to the trend of the data.

Table 5. Significance of the correlations between gas content, star formation and H_I disorder. The Pearson R coefficient is shown for each correlation, with the corresponding p-value in the following parenthesis. The values for the significant correlations (p-value < 0.05) are highlighted in bold. Correlations for primary galaxies are presented on the left while those for secondary galaxies are on the right.

	primary galaxies			secondary galaxies		
	$\Delta \log M_{\text{HI}}$	$\Delta \log M_{\text{HI,cor}}$	$\Delta \log SFR$	$\Delta \log M_{\text{HI}}$	$\Delta \log M_{\text{HI,cor}}$	$\Delta \log SFR$
$\Delta(\frac{F_{12}}{F_{123}})$	-0.07(0.86)	-0.24(0.56)	-0.40(0.32)	0.03(0.95)	0.02(0.95)	-0.51(0.20)
$\Delta(\frac{R_{12}}{F_{123}})$	-0.48(0.23)	-0.74(0.04)	-0.10(0.81)	-0.91(0.00)	-0.91(0.00)	-0.93(0.00)
$\Delta(\frac{F_{123}}{F_{\text{tot}}})$	-0.35(0.40)	-0.70(0.05)	-0.15(0.72)	-0.92(0.00)	-0.93(0.00)	-0.80(0.02)
$\Delta(\frac{F_{12}}{F_{\text{tot}}})$	-0.23(0.58)	-0.64(0.09)	-0.41(0.31)	-0.67(0.07)	-0.68(0.06)	-0.88(0.00)
$\Delta(\frac{R_{12}}{F_{12}})$	-0.76(0.03)	-0.69(0.06)	0.22(0.60)	-0.81(0.01)	-0.80(0.02)	-0.80(0.02)
$\Delta(\frac{R_{123}}{F_{123}})$	-0.54(0.17)	-0.66(0.08)	0.23(0.59)	-0.92(0.00)	-0.92(0.00)	-0.62(0.10)
$\Delta(f_{12}^+)$	-0.64(0.09)	-0.72(0.05)	0.03(0.95)	-0.80(0.02)	-0.78(0.02)	-0.86(0.01)
$\Delta(f_{123}^+)$	-0.64(0.09)	-0.63(0.09)	0.22(0.60)	-0.90(0.00)	-0.89(0.00)	-0.78(0.02)
$\Delta(S)$	-0.03(0.94)	-0.40(0.33)	-0.18(0.67)	-0.66(0.08)	-0.68(0.06)	-0.35(0.39)
$\Delta(L)$	-0.55(0.16)	-0.50(0.21)	0.30(0.47)	-0.94(0.00)	-0.94(0.00)	-0.55(0.16)

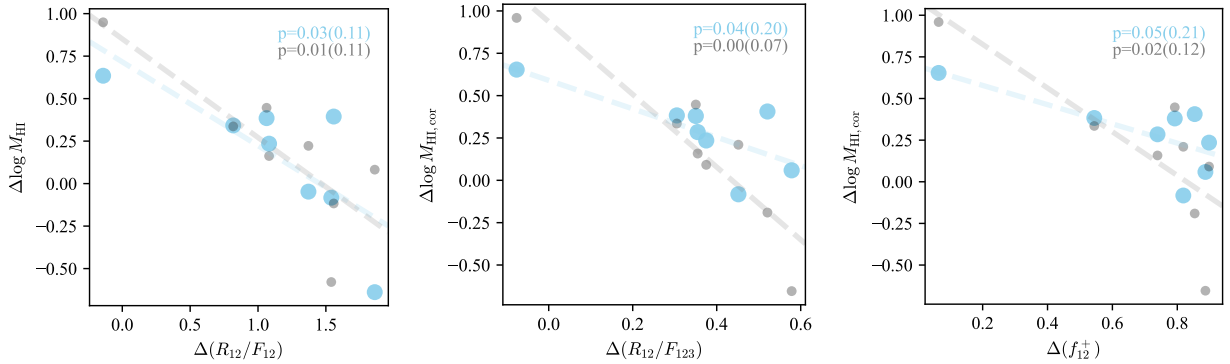


Figure 8. The anti-correlations between (corrected) H_I excess and different disorder parameters. Larger blue circles represent primary galaxies and smaller gray ones represent secondary galaxies. The p-values of correlations for primary (blue) and secondary (gray) galaxies are shown in the upper right corners with the bootstrap uncertainties in the following parenthesis. The dashed lines in different colors are linear fit to the corresponding data points, for guiding the eye to the trend of the data.

for primary galaxies with enhanced and suppressed integral SFR. We can see that the star formation suppressed primary galaxies have higher H_I surface densities outside the H_I disks. The H₂ surface density profiles are also presented for a subset of our sample for which CO image observations are available. We can see that the

primary galaxies have higher H₂ gas surface densities than typical star-forming galaxies (from THINGS, Leroy et al. 2008), which is mainly driven by the star formation enhanced ones.

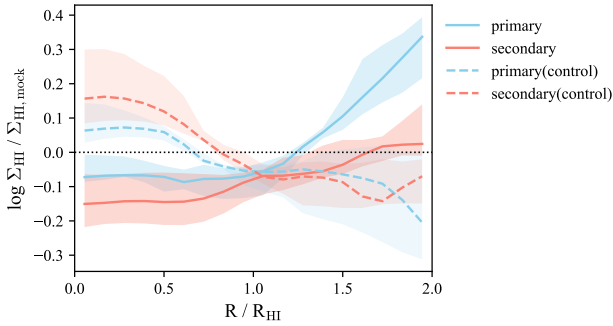


Figure 9. The median profiles of H I surface density ratio. Solid lines are used for interacting galaxies and dashed lines for the controls. The profiles of primary and secondary galaxies are plotted in blue and red, respectively. The shaded regions represent the uncertainties (15.9 and 84.1 percentile) of the corresponding profile.

5 DISCUSSION

5.1 Quantified relation between tidal strength and perturbed HI morphologies

Tidal interactions efficiently perturb and re-distribute H I of galaxies. H I tidal structures have frequently been found in previous studies, mostly based on interferometric H I images (e.g., [Hibbard & van Gorkom 1996](#)). We have quantitatively characterized tidally perturbed morphologies using a new set of morphological parameters (Figure 6), with new H I images that do not miss extended and low-column density H I, unlike the case for interferometric data (Appendix A).

We have shown with radial profiles in comparison to control galaxies (Figure 9) that the H I surface densities at large radius are enhanced for both primary and secondary galaxies. This is also indicated by the systematically larger $\Delta(L)$ parameters of the interacting sample in comparison to the control sample (Figure 6). A series of parameters quantifying the disorder of H I morphologies show that the interacting systems have systematically higher disorder in H I than the controls (Figure 6). We further showed in Figure 7 the dependence of $\Delta(S)$ and $\Delta(L)$ on relative velocity (e.g., [Barton et al. 2000](#); [Oh et al. 2008](#)) and mass ratio (e.g., [Ellison et al. 2008](#); [Bustamante et al. 2018](#)). It is likely that the strength of tidal interaction, which by theory is related to the galaxy mass ratio and orbits (e.g., [Toomre & Toomre 1972](#)), has determined the significance of H I tidal structures such as bridges and tails (e.g., [Mihos 2004](#)).

These results indicate that interacting systems have systematically larger expansion of H I than unperturbed systems, and the morphological parameters successfully characterize the significance of tidal perturbations.

We notice that the NGC4631-NGC4656 system is a significant outlier, for which the disorder parameters tend to be lower than the control galaxies in many cases (Figure 6). This is surprising, as most previous studies conclude this system as having experienced significant tidal perturbations (e.g., [Weliachew et al. 1978](#); [Rand 1994](#)). It is possibly because NGC4631-NGC4656 is the only interacting pair having both galaxies extremely inclined ($incl. > 80^\circ$). Moreover, most of the tidally perturbed H I lies between the two galaxies, which is likely due to the specific interacting orbits ([Combes 1978](#)), while most of the disorder parameters (e.g., f_{12}^+ , $\frac{R_{12}}{F_{12}}$, $\frac{R_{12}}{F_{12}}$ and $\frac{R_{12}}{F_{123}}$) are biased toward detecting signals beyond the line linking the pair galaxies. As a result, the disorder parameters may be insensitive to the perturbation levels exhibited in systems like the NGC4631-

NGC4656 pair. We leave such a caveat to future studies when more samples are available.

5.2 Do tidal interaction always induce enhanced SFR?

Theoretically, two basic neutral gas properties influence the SFR in galaxies — the distribution and the kinematics, which determine the amount of available material at star-forming regions, and whether star formation can efficiently happen with material on site, respectively ([Leroy et al. 2008](#); [Bigiel et al. 2008](#); [Bacchini et al. 2019a](#)). The tidal interaction influences both properties, by stripping the gas from both primary and secondary galaxies, and by compressing the gas and driving inflows ([Wang et al. 2022](#); [Scudder et al. 2012](#)).

It is clear that these H I-rich interacting galaxies are not always enhanced in their SFR (Section 3.3.3). In fact, almost all of the secondary galaxies have suppressed SFR. It seems that gas removal due to tidal stripping is dominantly more important than gas compression due to tidal shocks and ram pressure in these relatively low-mass galaxies. For primary galaxies, there is no significant correlation between the star formation rate enhancement and any H I disorder based on Pearson tests (Table 5). The majority of them (six out of eight) being star formation enhanced suggests that the possible dominant mechanism could be tidally induced gas compression and inflow in the inner disk increasing the inner-disk H₂ and total neutral gas surface densities (Figure 10). On the other hand, the significant anti-correlation between star formation rate enhancement and $\Delta(\frac{F_{12}}{F_{123}})$ based on Spearman test (Appendix F) suggests that the effects of gas removal due to tidal stripping may be non-negligible. The configuration and stage of interaction might also play a role in determining $\Delta \log SFR$ of the primary galaxies. These results demonstrate that, a statistical sample of spatially resolved gas images, and analysis of the gas distribution and kinematics are crucial for us to physically understand the suppression and enhancement in tidally interacting galaxies.

5.3 Does the tidal interaction deplete or accrete HI gas?

Table 5 show strong and/or significant anti-correlation between corrected H I excess and almost all H I disorder parameters for secondary galaxies, strongly supporting the relation between H I stripping and H I depletion in these minor galaxies in interactions. The H I excess or corrected H I excess also anti-correlates with several H I disorder parameters for primary galaxies based on Pearson test, and the simplest interpretation is that stronger tidal interactions also tend to deplete the H I in them. But the situation can be more complex than that for secondary galaxies.

Firstly, there is no significant correlation between (corrected) H I excess and any disorder parameter for primary galaxies based on Spearman or Kendall tests (Appendix F). Secondly, the significant Pearson correlations between H I disorders and corrected H I excess of primary galaxies are largely driven by the outlier NGC4631 (Figure 8). As discussed in Section 5.1, possibly due to a combined effect of inclination and encounter orbit, the disorder parameters may be insensitive to the perturbation level in this system. If we remove this galaxy from the sample, the correlation significance between $\Delta(\frac{R_{12}}{F_{123}})$, $\Delta(f_{12}^+)$ and corrected H I excess drops to 0.30 and 0.38, respectively. This is also indicated by the large uncertainty in p-value and non-correlations based on Spearman or Kendall tests (Appendix F). If the total neutral gas is actually independent from H I disorder, then a balance between the enhanced gas consumption (e.g., star formation) and increased rate of gas replenishment (e.g.,

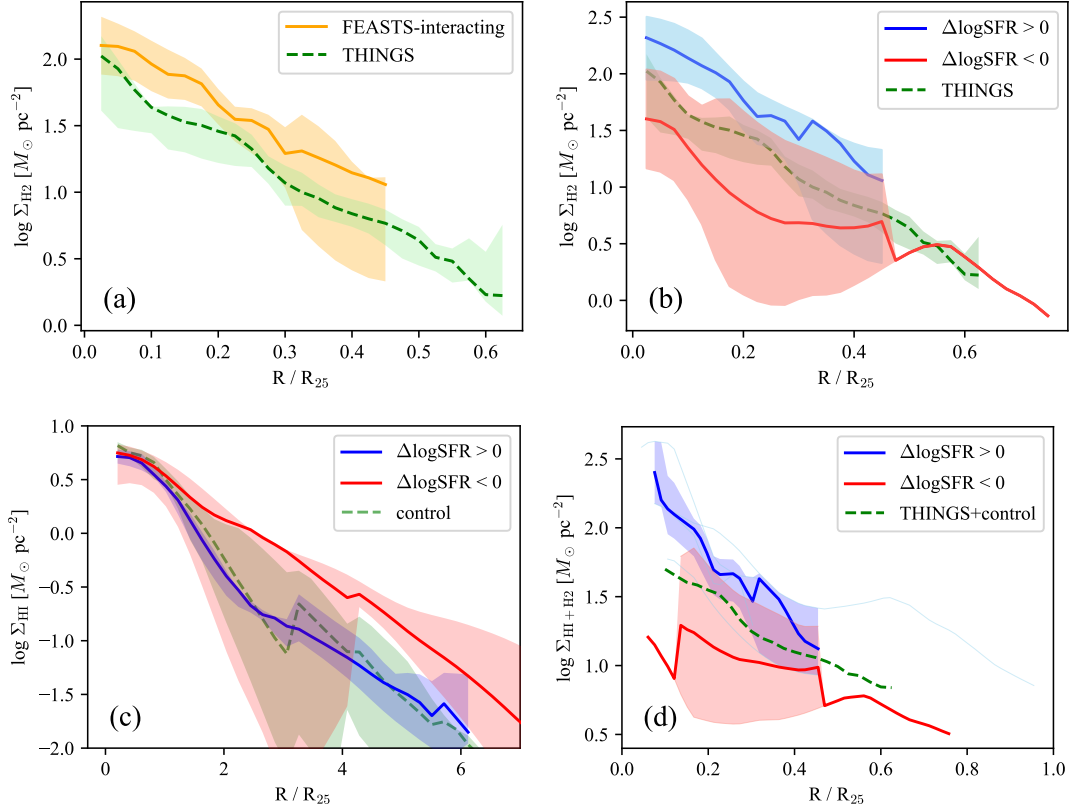


Figure 10. The gas surface density profiles of the primary galaxies and the corresponding controls. **Panel (a):** The median H_2 surface density profiles compared to THINGS galaxies (Leroy et al. 2008). **Panel (b):** The median H_2 surface density profiles of the star formation enhanced and suppressed galaxies compared to THINGS galaxies. **Panel (c):** The median H I surface density profiles of the star formation enhanced and suppressed galaxies compared to FEASTS isolated galaxies (Section 3.2.1). **Panel (d):** The median (in dark color) and individual (in light color) profiles of total neutral gas ($\text{H I} + \text{H}_2$) surface density compared to a virtual control produced by adding up the median H I profile of FEASTS isolated galaxies and H_2 profile of THINGS galaxies. Profiles of all, star formation enhanced and star formation suppressed primary galaxies are shown in orange, blue and red, respectively. The profiles of the corresponding controls are shown as green dashed curves. The shaded regions represent the uncertainties (15.9 and 84.1 percentile) of the profiles in the corresponding color.

accretion from CGM) is indicated. There are theoretical predictions that, CGM efficiently cools during tidal interaction, which happens at the significantly increased interface between H I and CGM through turbulence mixing and thermal conduction (Sparre et al. 2022). The theory is supported in several detailed case studies (Wang et al. 2023, Lin et al. in prep.).

Thirdly, gas accretion may happen at interaction stages not captured by those significantly correlated H I disorder parameters for primary galaxies. Statistical observational studies have been conducted in the literature, comparing mergers at different stages with control samples. They found H I enhancement in the post-merger sample (Ellison et al. 2015), and do not always find H I deficiency in the interacting sample (Zuo et al. 2018; Shangguan et al. 2019; Yu et al. 2022). The distinct fates of H I in the literature studies imply that the tidal depletion, star formation consumption, CGM cooling, H I inflow may dominate at different stages. In Table 5, the significant anti-correlations for the (corrected) H I excess are with the parameters describing the mass of H I being dragged outside H I disks onto the two ends ($\Delta(\frac{R_{12}}{F_{123}^+})$ and $\Delta(f_{12}^+)$), but not those describing the extents or clumpiness of H I ($\Delta(L)$ and $\Delta(S)$). A possible interpretation is that, H I is firstly depleted when a considerable fraction of H I is dragged out of H I disks, corresponding to the correlation between piling of H I at two ends of the system and H I deficiency. But later the situation changes when the perturbed H I expands to large areas, en-

larging the interface with the CGM and boosting the cooling (Wang et al. 2024; Sparre et al. 2022). If it was a one-way process for H I to be depleted after H I is dragged out H I disks, then a simple picture expected would be the H I becoming more deficient while expanding (i.e., next step of piling only at two ends of the system), and the morphology becoming more clumpy while H I evaporates and/or gets ionized. Neither trends are observed.

Besides, the causality between H I deficiency and piling of H I beyond H I disks may be the other way round, such that initially H I deficient systems tend to produce higher fraction of tidally stripped H I staying outside the initially unperturbed H I disk. This is possible because H I -poor galaxies having less extended H I disks tend to have weaker hydrodynamic effects (e.g. shocks and ram pressure) during interaction (Moon et al. 2019), and thus less inflow.

In summary, high level of H I (and neutral gas) deficiency seems to be associated with the mass fraction of H I stripping, while H I accretion may just start or be delayed to later stages when H I expands to large areas. Finally, we note that systematic uncertainties in separating H I into primary and secondary galaxies may affect the results.

6 SUMMARY AND CONCLUSION

In this work we investigate the fate of gas and star formation in interacting galaxies. Thanks to the FEASTS survey, we are able to fully map H I gas in the interacting systems down to column density of $\sim 10^{18} \text{ cm}^{-2}$ and physical scale up to $\sim 100 \text{ kpc}$. By building mocks and controls, we quantitatively describe disorder in H I morphology using a set of new morphological parameters. We further explore the effects of tidal interaction on the properties of H I, H₂ and the star formation rate of the interacting galaxies. Possible mechanisms that are responsible for influencing the gas reservoir and H I content, and those for causing star formation enhancement or suppression, are discussed. The key conclusions are as follows:

(i) Compared to a control sample, H I in interacting systems is distributed over a larger radius, has larger expansion, and preferentially accumulates at the opposing sides of the system. Such H I disorder is well characterized by the disorder parameters we defined. They show strong dependence on tidal interaction parameters stellar mass ratio and relative velocities between primary and secondary galaxies.

(ii) The generality of star formation suppression in the secondary galaxies points to the dominant effect of gas removal over induced compression and inflow during tidal interaction. While for the primary galaxies, star formation is more likely to be enhanced and independent from H I disorder.

(iii) The net consequence of a tidal interaction on the gas reservoir of the galaxies is a significant decrease in H I content and total neutral gas content for the secondary galaxies, while for the primary galaxies the relation is less strong or significant. These correlations strongly supporting the relation between tidal stripping and gas depletion in the secondary galaxies, and suggest a more complex situation for the primary galaxies.

The complex situation of the primary galaxies may relate to the different dominant effects at different stages of the interaction. Gas can firstly be depleted when it is dragged outside the H I disks, and later be enriched when accretion from CGM becomes dominant. Such speculation also partly explains the absence of significant correlation between star formation rate enhancement and H I disorder.

We note that the conclusions we reach in this work are largely based on a small sample of H I-rich galaxies. The dynamical range of the properties is rather limited. Whether the physical picture of gas depletion, accretion and star formation is valid in more general situations needs further testing. A more complete picture of the interplay between CGM, ISM and galaxy evolution in interacting systems will be further and better understood through combining with other multi-wavelength data and high-resolution hydrodynamic simulations.

ACKNOWLEDGEMENTS

We thank the anonymous referee for constructive comments. This work made use of the data from FAST (Five-hundred-meter Aperture Spherical radio Telescope)². FAST is a Chinese national mega-science facility, operated by National Astronomical Observatories, Chinese Academy of Sciences. JW thanks support of research grants from Ministry of Science and Technology of the People's Republic of China (NO. 2022YFA1602902), National Science Foundation of China (NO. 12073002, 12233001, 8200906879), and the China Manned Space Project. SW thanks Dr. Chen and Luna.

DATA AVAILABILITY

H I data from FEASTS will be published online³. All other data supporting this study is available from the corresponding author upon reasonable request.

REFERENCES

- Alonso M. S., Tissera P. B., Coldwell G., Lambas D. G., 2004, *MNRAS*, **352**, 1081
- Bacchini C., Fraternali F., Iorio G., Pezzulli G., 2019a, *A&A*, **622**, A64
- Bacchini C., Fraternali F., Pezzulli G., Marasco A., Iorio G., Nipoti C., 2019b, *A&A*, **632**, A127
- Bacchini C., Fraternali F., Pezzulli G., Marasco A., 2020, *A&A*, **644**, A125
- Barnes D. G., et al., 2001, *MNRAS*, **322**, 486
- Barton E. J., Geller M. J., Kenyon S. J., 2000, *ApJ*, **530**, 660
- Bigiel F., Leroy A., Walter F., Brinks E., de Blok W. J. G., Madore B., Thornley M. D., 2008, *AJ*, **136**, 2846
- Bok J., Blyth S. L., Gilbank D. G., Elson E. C., 2019, *MNRAS*, **484**, 582
- Bustamante S., Sparre M., Springel V., Grand R. J. J., 2018, *MNRAS*, **479**, 3381
- Bustamante S., Ellison S. L., Patton D. R., Sparre M., 2020, *MNRAS*, **494**, 3469
- Cao C., et al., 2016, *ApJS*, **222**, 16
- Catinella B., et al., 2018, *MNRAS*, **476**, 875
- Chown R., et al., 2019, *MNRAS*, **484**, 5192
- Combes F., 1978, *A&A*, **65**, 47
- Di Teodoro E. M., Fraternali F., 2015, *MNRAS*, **451**, 3021
- Ellison S. L., Patton D. R., Simard L., McConnachie A. W., 2008, *AJ*, **135**, 1877
- Ellison S. L., Patton D. R., Simard L., McConnachie A. W., Baldry I. K., Mendel J. T., 2010, *MNRAS*, **407**, 1514
- Ellison S. L., Patton D. R., Mendel J. T., Scudder J. M., 2011, *MNRAS*, **418**, 2043
- Ellison S. L., Mendel J. T., Patton D. R., Scudder J. M., 2013, *MNRAS*, **435**, 3627
- Ellison S. L., Fertig D., Rosenberg J. L., Nair P., Simard L., Torrey P., Patton D. R., 2015, *MNRAS*, **448**, 221
- Ellison S. L., Catinella B., Cortese L., 2018, *MNRAS*, **478**, 3447
- Elmegreen D. M., Sundin M., Elmegreen B., Sundelius B., 1991, *A&A*, **244**, 52
- Fouque P., Bottinelli L., Gouguenheim L., Patrel G., 1990, *ApJ*, **349**, 1
- Fujita Y., 1998, *ApJ*, **509**, 587
- Garduño L. E., Lara-López M. A., López-Cruz O., Hopkins A. M., Owers M. S., Pimblet K. A., Holwerda B. W., 2021, *MNRAS*, **501**, 2969
- Gnedin O. Y., 2003, *ApJ*, **582**, 141
- Haynes M. P., et al., 2018, *ApJ*, **861**, 49
- Heald G., et al., 2011, *A&A*, **526**, A118
- Helfer T. T., Thornley M. D., Regan M. W., Wong T., Sheth K., Vogel S. N., Blitz L., Bock D. C. J., 2003, *ApJS*, **145**, 259
- Hess K. M., Cluver M. E., Yahya S., Leisman L., Serra P., Lucero D. M., Passmoor S. S., Carignan C., 2017, *MNRAS*, **464**, 957
- Hibbard J. E., van Gorkom J. H., 1996, *AJ*, **111**, 655
- Hickson P., 1982, *ApJ*, **255**, 382
- Huchtmeier W. K., 1997, *A&A*, **325**, 473
- Irwin J. A., 1994, *ApJ*, **429**, 618
- Janowiecki S., Catinella B., Cortese L., Saintonge A., Wang J., 2020, *MNRAS*, **493**, 1982
- Jones M. G., et al., 2019, *A&A*, **632**, A78
- Lambas D. G., Tissera P. B., Alonso M. S., Coldwell G., 2003, *MNRAS*, **346**, 1189
- Lambas D. G., Alonso S., Mesa V., O'Mill A. L., 2012, *A&A*, **539**, A45
- Lee-Waddell K., Spekkens K., Haynes M. P., Stierwalt S., Chengalur J., Chandra P., Giovanelli R., 2012, *MNRAS*, **427**, 2314

² <https://cstr.cn/31116.02.FAST>

³ <https://github.com/FEASTS/LVgal/wiki>

Lee-Waddell K., et al., 2016, *MNRAS*, **460**, 2945

Lelli F., McGaugh S. S., Schombert J. M., 2016, *AJ*, **152**, 157

Leroy A. K., Walter F., Brinks E., Bigiel F., de Blok W. J. G., Madore B., Thornley M. D., 2008, *AJ*, **136**, 2782

Leroy A. K., et al., 2009, *AJ*, **137**, 4670

Leroy A. K., et al., 2019, *ApJS*, **244**, 24

Martinez-Badenes V., Lisenfeld U., Espada D., Verdes-Montenegro L., García-Burillo S., Leon S., Sulentic J., Yun M. S., 2012, *A&A*, **540**, A96

Mihos J. C., 2004, in Duc P.-A., Braine J., Brinks E., eds, IAU Symposium Vol. 217, Recycling Intergalactic and Interstellar Matter. p. 390 ([arXiv:astro-ph/0401557](https://arxiv.org/abs/astro-ph/0401557)), doi:10.48550/arXiv.astro-ph/0401557

Moon J.-S., An S.-H., Yoon S.-J., 2019, *ApJ*, **882**, 14

Oh S. H., Kim W.-T., Lee H. M., Kim J., 2008, *ApJ*, **683**, 94

Pan H.-A., et al., 2018, *ApJ*, **868**, 132

Pan H.-A., et al., 2019, *ApJ*, **881**, 119

Pearson S., et al., 2016, *MNRAS*, **459**, 1827

Rand R. J., 1994, *A&A*, **285**, 833

Saintonge A., et al., 2016, *MNRAS*, **462**, 1749

Saintonge A., et al., 2017, *ApJS*, **233**, 22

Schechtman-Rook A., Bershadsky M. A., 2014, *ApJ*, **795**, 136

Schruba A., et al., 2012, *AJ*, **143**, 138

Scudder J. M., Ellison S. L., Torrey P., Patton D. R., Mendel J. T., 2012, *MNRAS*, **426**, 549

Scudder J. M., Ellison S. L., Momjian E., Rosenberg J. L., Torrey P., Patton D. R., Fertig D., Mendel J. T., 2015, *MNRAS*, **449**, 3719

Serra P., et al., 2015, *MNRAS*, **448**, 1922

Shangguan J., Ho L. C., Li R., Zhuang M.-Y., Xie Y., Li Z., 2019, *ApJ*, **870**, 104

Sheth K., et al., 2010, *PASP*, **122**, 1397

Smith B. J., Wagstaff P., Struck C., Soria R., Dunn B., Swartz D., Giroux M. L., 2019, *AJ*, **158**, 169

Sorai K., et al., 2019, *PASJ*, **71**, S14

Sparre M., Whittingham J., Damle M., Hani M. H., Richter P., Ellison S. L., Pfrommer C., Vogelsberger M., 2022, *MNRAS*, **509**, 2720

Thorp M. D., Ellison S. L., Simard L., Sánchez S. F., Antonio B., 2019, *MNRAS*, **482**, L55

Toomre A., Toomre J., 1972, *ApJ*, **178**, 623

Verdes-Montenegro L., Yun M. S., Perea J., del Olmo A., Ho P. T. P., 1998, *ApJ*, **497**, 89

Verdes-Montenegro L., Yun M. S., Williams B. A., Huchtmeier W. K., Del Olmo A., Perea J., 2001, *A&A*, **377**, 812

Violino G., Ellison S. L., Sargent M., Coppin K. E. K., Scudder J. M., Mendel T. J., Saintonge A., 2018, *MNRAS*, **476**, 2591

Walter F., Brinks E., de Blok W. J. G., Bigiel F., Kennicutt Robert C. J., Thornley M. D., Leroy A., 2008, *AJ*, **136**, 2563

Wang J., Koribalski B. S., Serra P., van der Hulst T., Roychowdhury S., Kamphuis P., Chengalur J. N., 2016, *MNRAS*, **460**, 2143

Wang J., Catinella B., Saintonge A., Pan Z., Serra P., Shao L., 2020, *ApJ*, **890**, 63

Wang S., et al., 2022, *ApJ*, **927**, 66

Wang J., et al., 2023, *ApJ*, **944**, 102

Wang J., et al., 2024, *ApJ*, **968**, 48

Weliachew L., Sancisi R., Guélin M., 1978, *A&A*, **65**, 37

Wetzel A. R., Tinker J. L., Conroy C., van den Bosch F. C., 2013, *MNRAS*, **432**, 336

Williams B. A., Rood H. J., 1987, *ApJS*, **63**, 265

Woods D. F., Geller M. J., 2007, *AJ*, **134**, 527

Yu Q., Fang T., Feng S., Zhang B., Xu C. K., Wang Y., Hao L., 2022, *ApJ*, **934**, 114

Zuo P., Xu C. K., Yun M. S., Lisenfeld U., Li D., Cao C., 2018, *ApJS*, **237**, 2

de Vaucouleurs G., de Vaucouleurs A., Corwin Herold G. J., Buta R. J., Paturel G., Fouque P., 1991, Third Reference Catalogue of Bright Galaxies. Springer, New York, NY (USA)

APPENDIX A: CHANNEL AND MOMENT-0 MAPS COMPARED TO PREVIOUS OBSERVATIONS

In Figure A1 we compare the channel maps of the NGC3169-NGC3166 system from the FEASTS data cube and those from the ALFALFA data cube. Similarly the channel maps of the NGC4725-NGC4747 system from FEASTS and ALFALFA are presented in Figure A2. The FEASTS channel maps are interpolated to match the velocities of the ALFALFA data cube. The field-of-view and color scales are identical between different data of the same system. The rms level of FEASTS data cube is significantly lower than that of the ALFALFA data cube. Thus FEASTS data cube reveals more faint structures than ALFALFA. The spatial resolution of FEASTS is also better, showing significantly more details of the H_I morphology across different velocity slices.

In Figure A3 we present the moment-0 map of the NGC3169-NGC3166 system from FEASTS and that from GMRT. The moment-0 maps of the NGC4725-NGC4747 system are shown in Figure A4. The source masks for the GMRT data cubes are constructed using *SoFiA* similarly as for the FEASTS data cubes (Section 3.1.1). The field-of-view and color scales are identical between different data of the same system. FEASTS moment-0 maps reveal significantly more H_I fluxes and structures at larger galactic radii. They effectively capture the faint and/or large-scale components which are severely missed by GMRT observations. Though lacking small-scale resolution compared to interferometry data, FEASTS moment-0 maps well probe the spatial distribution of H_I in tidally interacting galaxies with better completeness.

APPENDIX B: HI FLUX DIVISION

The H_I components of small galaxies are identified via visual inspection on both H_I moment-0 maps and optical images. We identify one small clump of H_I component belong to a small galaxy in each of M77-NGC1055, NGC4725-NGC4747, NGC3169-NGC3166 and NGC5775-NGC5774 systems.

Following Wang et al. (2023) and Huang et al. (in prep.), we use the python function *watershed* from the *skimage.segmentation* module to divide pixels that belongs to the small component from those belong to the major members of the interacting systems. Firstly, we use python function *peak_local_max* from *skimage.feature* module to locate local peaks of the H_I fluxes in moment-0 maps. Secondly, we adjust the number of peaks to be found so that the small component is located. Then we perform segmentation based on the local peaks via *watershed*. Finally, all segments other than that of the small component are combined. So that the moment-0 maps are segmented into two parts – main component of H_I that are connected to the major members of the interacting system, and the minor component of H_I connected to the small galaxies nearby.

We do not perform segmentation in cube domain because the well resolved complex and irregular H_I structure in these interacting systems makes it difficult to separate the fluxes.

APPENDIX C: MOCK HI PROFILE ADJUSTMENT

The use of H_I size-mass relation and the universal H_I profile do not automatically produce self-consistent H_I disks. I.e., the integrated H_I flux of the produced H_I profile would not be equal to the H_I mass that we input at the beginning. There are two reasons causing the inconsistency. The first reason is that the universal profile is derived as the median of the profiles of individual galaxies. This derivation

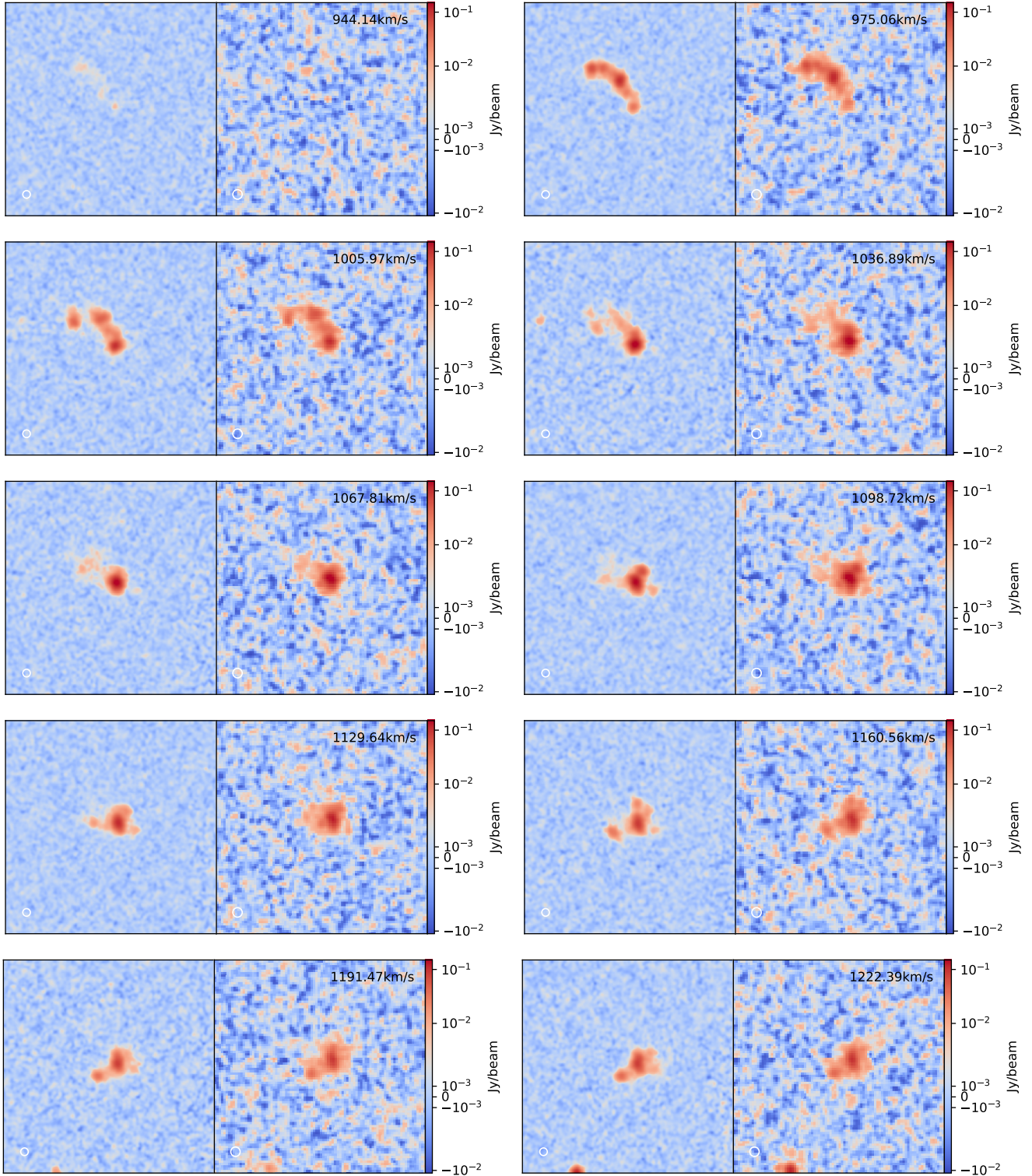


Figure A1. The channel maps of the NGC3169-NGC3166 system from FEASTS (left panels) and ALFALFA (right panels). The velocity of the channel is shown in the upper right corner. The beams are shown as the empty circles in the lower left corner in each panel.

does not guarantee flux conservation. The second reason is that the slope of the H_I size-mass relation is not accurately 0.5. The non-zero deviation of the actual slope from 0.5 determines that the H_I disks are not strictly self-similar. Considering that the inconsistency caused by the two facts are both small compared to the large intrinsic

uncertainty in the inner region of the universal H_I profiles, we decide to adjust the profile in the inner region so that consistency is achieved. The H_I size-mass relation, on the other hand, is not changed.

We perform the adjustment as a function of the input H_I mass. Firstly, an original H_I profile is produced as illustrated in Sec-

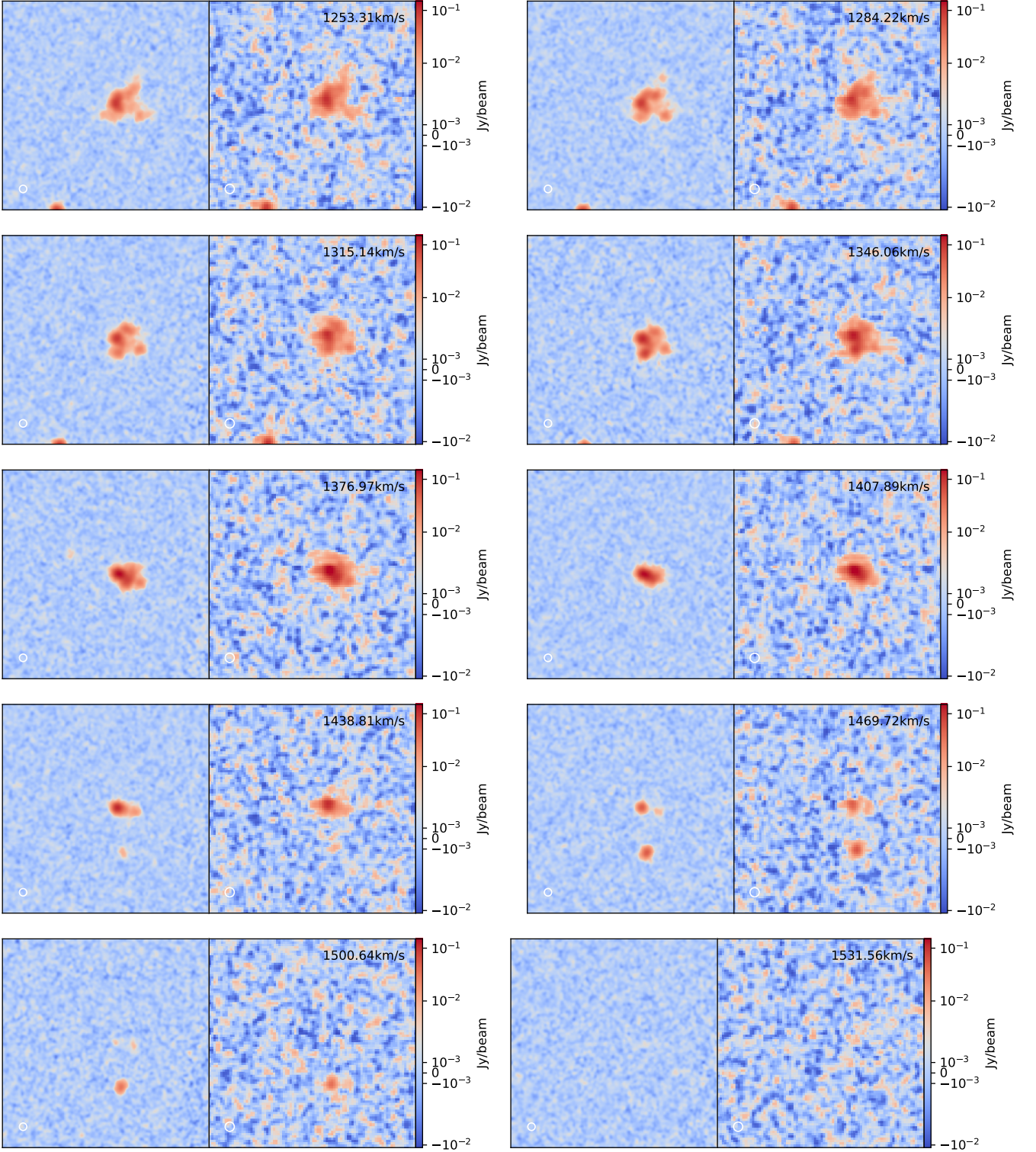


Figure A1 – continued

tion 3.3.2. By integrating the H I profile as a function of radius, we calculate the integrated H I mass of the profile and the deviation from the initial H I mass we input. Then we construct a half-Gaussian centered on $R = 0$ extending only to $R > 0$. The dispersion of it is set to be $\sigma = 0.2R_{\text{HI}}$. And its amplitude is determined so that it integrates to the H I mass deviation. Finally this half-Gaussian is

added to the original H I profile and we obtain the adjusted H I profile which integrates to the exactly same amount of H I mass as the input.

The differences of the integrated H I mass between the original and the adjusted H I profile vary from $\sim 2\%$ to $\sim 6\%$ as a function of the input H I mass.

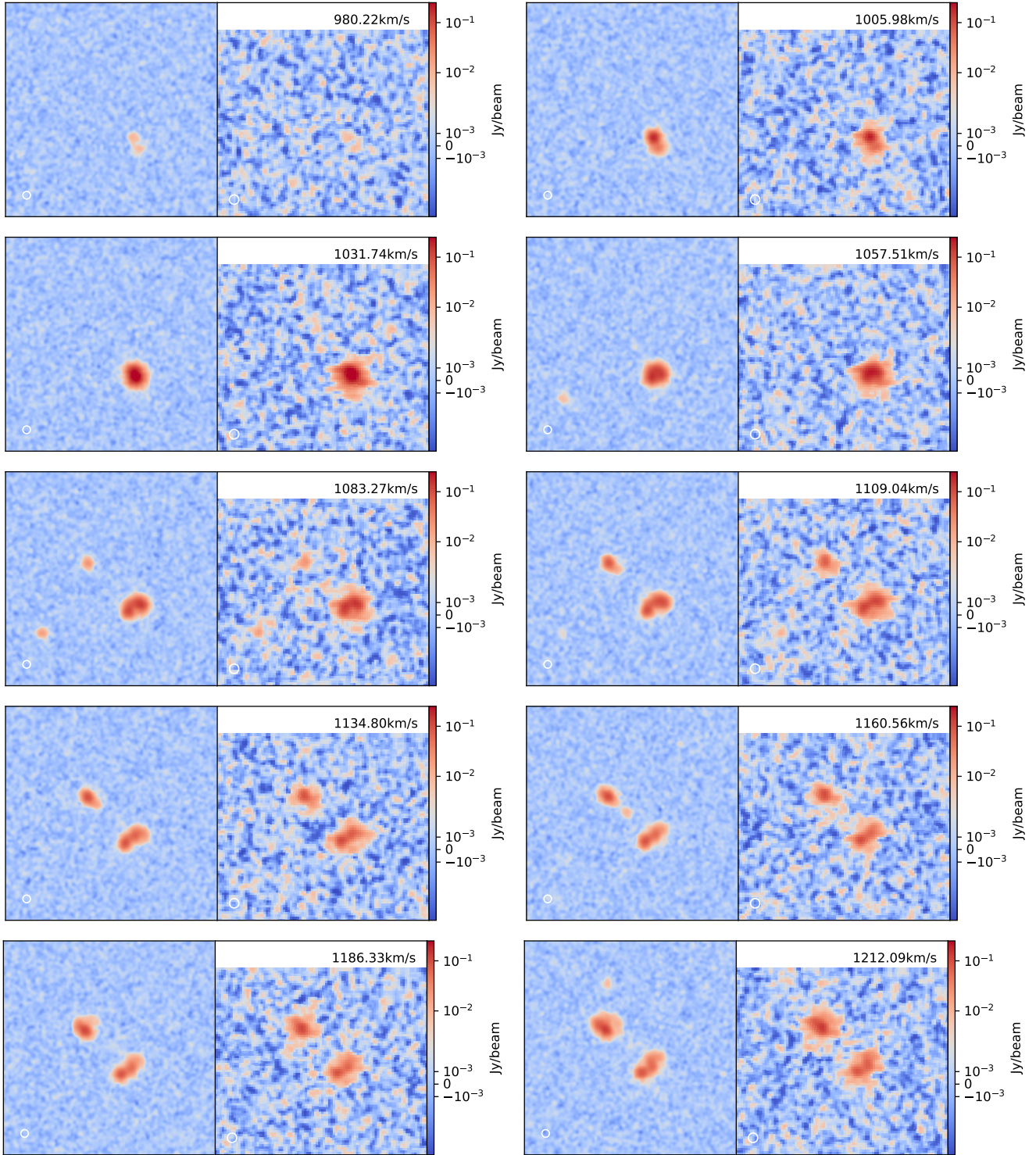


Figure A2. The channel maps of the NGC4725-NGC4747 system from FEASTS (left panels) and ALFALFA (right panels). The velocity of the channel is shown in the upper right corner. The beams are shown as the empty circles in the lower left corner in each panel.

APPENDIX D: COMPARISON OF HI PSD BETWEEN INTERACTING SYSTEMS AND MOCK

We compare the HI flux distribution of real and mock galaxies in an order of increasing significance of tidal structures seen in HI PSD (Figure 2):

- We see extraplanar structures beyond the outermost (red, 99.7%) contour of M77-NGC1055, NGC4725-NGC4747 and NGC672-IC1727. Within the outermost contour, the rotation configuration of the main HI disk is largely maintained.

- The HI disks of primary and secondary galaxies are clearly connected by a considerable amount of HI in the NGC4631-NGC4656

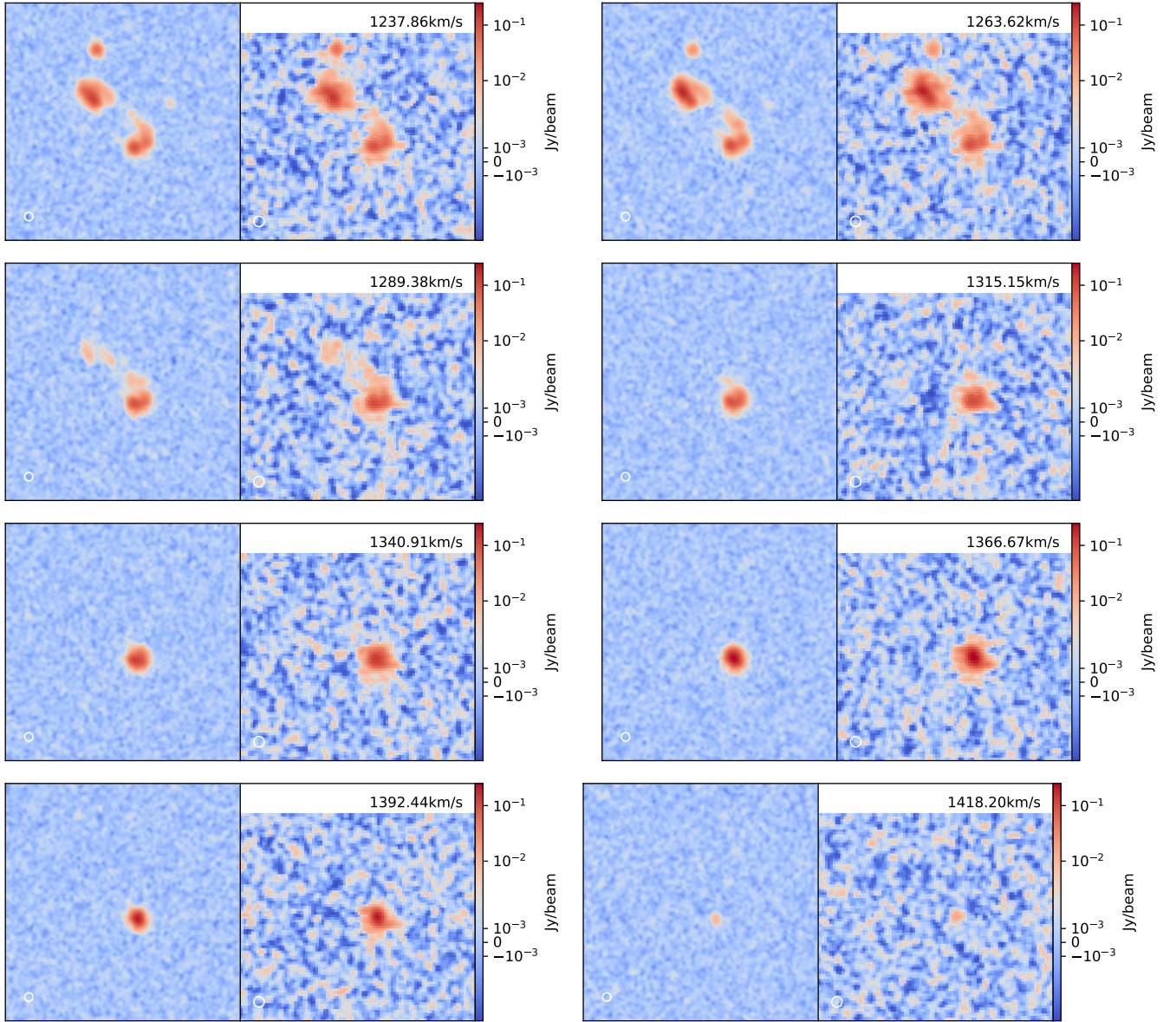


Figure A2 – continued

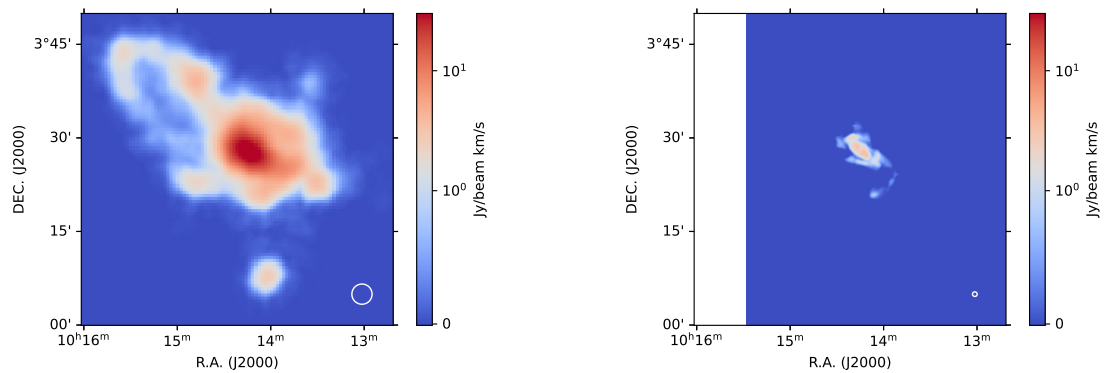


Figure A3. The moment-0 maps of the NGC3169-NGC3166 system from FEASTS (left panel) and from GMRT (right panel). The beam is shown as the empty circle in the lower right corner.

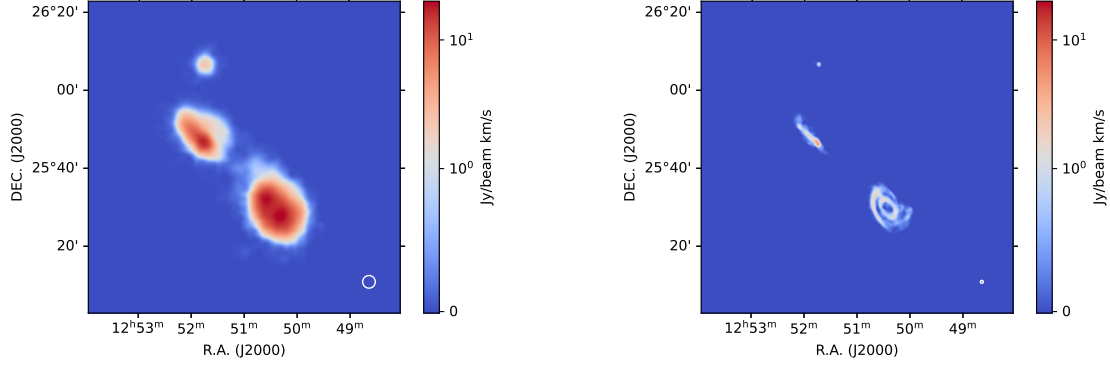


Figure A4. The moment-0 maps of the NGC4725-NGC4747 system from FEASTS (left panel) and from GMRT (right panel). The beam is shown as the empty circle in the lower right corner.

and NGC660-IC0148 systems. The rotation configuration of the main H_I disks is also affected.

- The H_I in the NGC3169-NGC3166 and NGC5194-NGC5195 systems forms a large envelope surrounding both galaxies. The H_I component of the secondary galaxies can not be clearly distinguished from that of the primary galaxy or the envelope. There is also a significant amount of H_I outside the envelopes with l-o-s velocities which are mostly consistent with the H_I disks.

- The observation of the NGC5775-NGC5774 system is limited by the resolution. There is little H_I beyond the outermost contour. Projection effect cause the H_I components of the two galaxies to overlap with each other significantly. We suspect it is in a similar state to the NGC672-IC1727 system but with weaker tidal interaction.

APPENDIX E: RESIDUAL MAPS OF THE CONTROLS

In Figure E1 we present the residual maps of the controls. For each interacting system, a representative example is shown.

APPENDIX F: CORRELATIONS EVALUATED BY SPEARMAN AND KENDALL TESTS

In Table F1 we present the Spearman R coefficients and p-values for all the combinations of correlations as in Table 5. And the Kendall τ coefficients and p-values are presented in Table F2. For primary galaxies, there is no significant correlation for the H_I excess ($\Delta \log M_{\text{HI}}$) or corrected H_I excess ($\Delta \log M_{\text{HI,cor}}$). The only significant correlation is between star formation rate enhancement and $\Delta(\frac{F_{12}}{F_{123}})$ based on Spearman test. For secondary galaxies, both H_I excess and corrected H_I excess significantly anti-correlate with $\Delta(\frac{R_{12}}{F_{123}})$, $\Delta(\frac{F_{123}}{F_{\text{tot}}})$, $\Delta(\frac{R_{12}}{F_{12}})$, $\Delta(f_{12}^+)$, $\Delta(f_{123}^+)$ and $\Delta(L)$. The star formation rate enhancement also show significant anti-correlations with $\Delta(\frac{R_{12}}{F_{123}})$, $\Delta(\frac{F_{123}}{F_{\text{tot}}})$ and $\Delta(\frac{F_{12}}{F_{\text{tot}}})$ based on Spearman tests, and with $\Delta(\frac{F_{123}}{F_{\text{tot}}})$ and $\Delta(\frac{F_{12}}{F_{\text{tot}}})$ based on Kendall tests.

This paper has been typeset from a $\text{\TeX}/\text{\LaTeX}$ file prepared by the author.

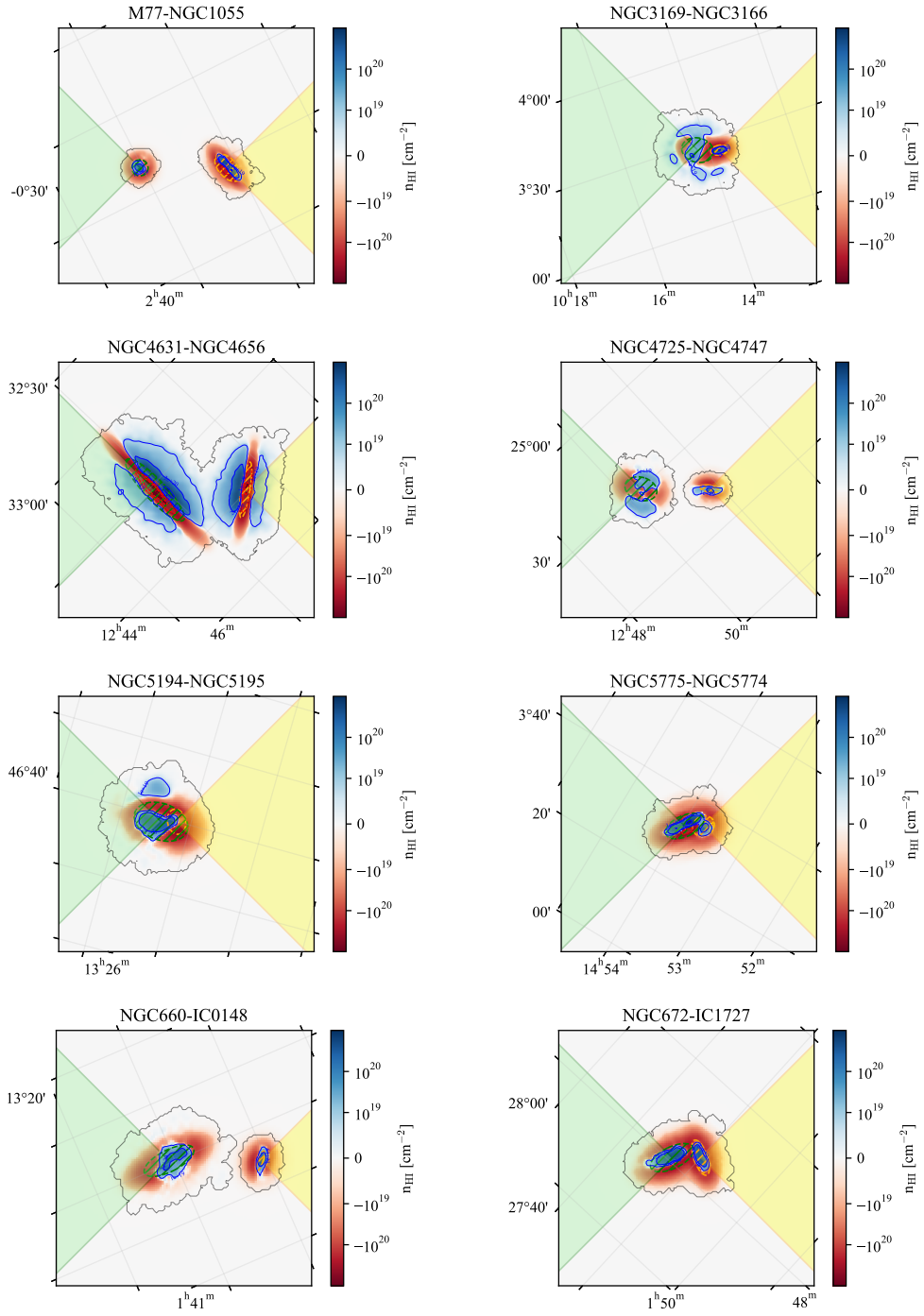


Figure E1. The rotated residual maps of the controls. All symbols are the same as those in Figure 5.

Table F1. Significance of the correlations between gas content, star formation and H I disorder. The Spearman R coefficient is shown for each correlation, with the corresponding p-value in the following parenthesis. The values for the significant correlations (p-value < 0.05) are highlighted in bold. Correlations for primary galaxies are presented on the left while those for secondary galaxies are on the right.

	primary galaxies			secondary galaxies		
	$\Delta \log M_{\text{HI}}$	$\Delta \log M_{\text{HI,cor}}$	$\Delta \log SFR$	$\Delta \log M_{\text{HI}}$	$\Delta \log M_{\text{HI,cor}}$	$\Delta \log SFR$
$\Delta(\frac{F_{12}}{F_{123}})$	0.10(0.82)	-0.17(0.69)	-0.71(0.05)	0.02(0.96)	0.02(0.96)	-0.50(0.21)
$\Delta(\frac{R_{12}}{F_{123}})$	-0.52(0.18)	-0.60(0.12)	0.10(0.82)	-0.90(0.00)	-0.90(0.00)	-0.76(0.03)
$\Delta(\frac{F_{123}}{F_{\text{tot}}})$	-0.45(0.26)	-0.57(0.14)	0.05(0.91)	-0.88(0.00)	-0.88(0.00)	-0.83(0.01)
$\Delta(\frac{F_{12}}{F_{\text{tot}}})$	-0.19(0.65)	-0.43(0.29)	-0.33(0.42)	-0.67(0.07)	-0.67(0.07)	-0.93(0.00)
$\Delta(\frac{R_{12}}{F_{12}})$	-0.62(0.10)	-0.50(0.21)	0.31(0.46)	-0.86(0.01)	-0.86(0.01)	-0.45(0.26)
$\Delta(\frac{R_{123}}{F_{123}})$	-0.67(0.07)	-0.40(0.32)	0.57(0.14)	-0.69(0.06)	-0.69(0.06)	-0.26(0.53)
$\Delta(f_{12}^+)$	-0.69(0.06)	-0.60(0.12)	0.31(0.46)	-0.81(0.01)	-0.81(0.01)	-0.36(0.39)
$\Delta(f_{123}^+)$	-0.62(0.10)	-0.48(0.23)	0.52(0.18)	-0.90(0.00)	-0.90(0.00)	-0.36(0.39)
$\Delta(S)$	-0.17(0.69)	-0.33(0.42)	0.07(0.87)	-0.69(0.06)	-0.69(0.06)	-0.69(0.06)
$\Delta(L)$	-0.55(0.16)	-0.48(0.23)	0.38(0.35)	-0.98(0.00)	-0.98(0.00)	-0.60(0.12)

Table F2. Significance of the correlations between gas content, star formation and H I disorder. The Kendall τ coefficient is shown for each correlation, with the corresponding p-value in the following parenthesis. The values for the significant correlations (p-value < 0.05) are highlighted in bold. Correlations for primary galaxies are presented on the left while those for secondary galaxies are on the right.

	primary galaxies			secondary galaxies		
	$\Delta \log M_{\text{HI}}$	$\Delta \log M_{\text{HI,cor}}$	$\Delta \log SFR$	$\Delta \log M_{\text{HI}}$	$\Delta \log M_{\text{HI,cor}}$	$\Delta \log SFR$
$\Delta(\frac{F_{12}}{F_{123}})$	0.07(0.90)	-0.07(0.90)	-0.57(0.06)	0.00(1.00)	0.00(1.00)	-0.36(0.28)
$\Delta(\frac{R_{12}}{F_{123}})$	-0.43(0.18)	-0.57(0.06)	0.07(0.90)	-0.79(0.01)	-0.79(0.01)	-0.57(0.06)
$\Delta(\frac{F_{123}}{F_{\text{tot}}})$	-0.36(0.28)	-0.50(0.11)	0.00(1.00)	-0.71(0.01)	-0.71(0.01)	-0.64(0.03)
$\Delta(\frac{F_{12}}{F_{\text{tot}}})$	-0.14(0.72)	-0.43(0.18)	-0.21(0.55)	-0.50(0.11)	-0.50(0.11)	-0.86(0.00)
$\Delta(\frac{R_{12}}{F_{12}})$	-0.57(0.06)	-0.43(0.18)	0.21(0.55)	-0.64(0.03)	-0.64(0.03)	-0.43(0.18)
$\Delta(\frac{R_{123}}{F_{123}})$	-0.50(0.11)	-0.36(0.28)	0.43(0.18)	-0.57(0.06)	-0.57(0.06)	-0.21(0.55)
$\Delta(f_{12}^+)$	-0.57(0.06)	-0.43(0.18)	0.21(0.55)	-0.64(0.03)	-0.64(0.03)	-0.29(0.40)
$\Delta(f_{123}^+)$	-0.43(0.18)	-0.43(0.18)	0.36(0.28)	-0.79(0.01)	-0.79(0.01)	-0.29(0.40)
$\Delta(S)$	-0.14(0.72)	-0.29(0.40)	0.07(0.90)	-0.50(0.11)	-0.50(0.11)	-0.43(0.18)
$\Delta(L)$	-0.43(0.18)	-0.43(0.18)	0.21(0.55)	-0.93(0.00)	-0.93(0.00)	-0.43(0.18)